Title: **Integrated Thermal and Phyto-Remediation of Agricultural Soils Impacted by PFAS**

Authors: Jake T Thompson[1], Millie Dobson[2], Tim Jesper Suhrhoff[3], Yoshiki Kanzaki[4], Chloe Kent[1], Lucinda Bryce[5], Rachel James[2], Ella Milliken[1], Christopher T Reinhard[4], Noah Planavsky[1]*

Affiliations:

[1]Department of Earth and Planetary Sciences, Yale University, 10 Whitney Ave., New Haven CT 06511 USA

[2]School of Ocean and Earth Science, National Oceanography Centre Southampton, University of Southampton Waterfront Campus, Southampton SO14 3ZH, UK

[3]Yale Center for Natural Carbon Capture, Yale University, New Haven, Connecticut 06511, USA

[4]School of Earth & Atmospheric Sciences, Georgia Institute of Technology, Atlanta, Georgia 30332, USA

[5]Department of Earth, Environmental, and Planetary Sciences, Brown University, Providence, Rhode Island 02912, USA

* Corresponding author. email: noah.planavsky@yale.edu

Abstract: Widespread biosolids application has introduced per- and polyfluoroalkyl substances (PFAS) into millions of hectares of agricultural soils, yet existing remediation methods are costly, carbon intensive, and impractical at scale. We evaluate an integrated strategy that combines phytoremediation, biomass pyrolysis, and enhanced weathering to remove PFAS while generating durable carbon dioxide removal. Using stochastic modeling constrained by experimental data, we show that raising soil pH with alkaline rock amendments increases PFAS mobility and plant uptake, shortening remediation timelines by more than a decade under typical contamination levels. National-scale simulations across ~1 million hectares of contaminated cropland yield a combined carbon dioxide removal potential of ~12 Mt CO_2 yr^{-1}. Remediation costs of ~1,300 USD ha^{-1} yr^{-1} are over an order of magnitude lower than conventional approaches.

Main Text:

Per- and polyfluoroalkyl substances (PFAS) are a large class of synthetic chemicals which have become ubiquitous in consumer and industrial applications (*1*, *2*). Their persistence in the environment has earned them the label "forever chemicals." Nearly all people now have detectable levels of PFAS in their blood (*3–5*), and exposure has been linked to cancer, liver damage, thyroid disease, immune dysfunction, and reproductive disorders(*6*, *7*). Because PFAS resist natural degradation, they accumulate in soils and water once released, posing long-term risks to human health and ecosystems(*8*, *9*).

Decades of widespread PFAS use have led to their release into wastewater(*10*), where they concentrate in sewage sludges, also known as biosolids(*8*, *11*, *12*). These biosolids, often applied to farmland as a nutrient-rich fertilizer, represent a major pathway for PFAS to enter agricultural soils, groundwater, and the food system. This is a nearly worldwide problem, but one that has recently emerged as a key policy priority in the United States. A recent U.S. Environmental Protection Agency risk assessment showed that perfluorooctane sulfonic acid (PFOS) and perfluorooctanoic acid (PFOA) in biosolids can exceed human health thresholds at typical biosolid application rates(*13*). States such as Maine have already shut down farms where PFAS levels surpassed regulatory limits, highlighting the growing challenge these contaminants pose for agricultural communities(*14*, *15*).

Remediating PFAS-contaminated farmland is currently infeasible at scale. Established methods—thermal destruction or excavation and landfilling—cost an estimated $0.8–1.6 million per hectare(*16*). With over a million hectares of U.S. farmland likely affected by biosolids use(*17*), remediation costs could run into the trillions of dollars using traditional approaches. Beyond cost, these methods strip away topsoil and release large quantities of carbon dioxide. A

scalable, sustainable, and cost-effective approach toward remediating PFAS-contaminated farmland is urgently needed.

Here, we present and evaluate the feasibility, impacts, and cost of a remediation strategy that integrates phytoremediation paired with soil pH management and biochar production. This combined approach aims to accelerate PFAS removal from soil, immobilize residual contamination, and restore farmland while simultaneously achieving durable carbon dioxide removal. We provide the first quantitative assessment of the remediation potential, costs, and scalability of this strategy across U.S. croplands, offering a potential path toward addressing a pressing environmental challenge over the coming decades.

Remediation pathway

Our proposed remediation method operates in two stages. First, the application of alkaline rock amendments to soil (or enhanced weathering) elevates soil pH, leading to an increase in mobility(*18*) and bioavailability(*19*) of key PFAS compounds such as perfluorooctane sulfonate (PFOS) and perfluorooctanoic acid (PFOA). Next, the PFAS-containing biomass is pyrolyzed with the off-gas being oxidized, effectively destroying PFAS through thermal degradation(*20–22*) while generating biochar. The biochar is then readded to soils or transported to sites where PFAS contamination is too high to be addressed with phytoremediation alone. Biochar has been shown to be effective at immobilizing PFOS, able to achieve 99% reduction in leaching in soils at application rates as low as 1–5% by mass(*23*). The biochar therefore provides a means to limit PFAS transfer into well waters. With continued application, the ratio of biochar to contaminated soil increases, further reducing PFAS bioavailability by competitive sorption(*9*, *23*, *24*). In addition to remediating soils, both addition of biochar to soils(*25*) and enhanced weathering (*26*) are promising nature-based approaches to remove carbon dioxide from the atmosphere and

reduce greenhouse gas emissions from crop system such that this pathway represents a multifunctional approach where environmental remediation and climate change mitigation can be addressed synergistically and be used to potentially cross-finance each other.

This dual extraction and immobilization approach allows for a significant degree of flexibility—at sites where PFAS concentrations are relatively low and regulatory thresholds are within reach, enhanced weathering can accelerate phytoremediation to meet soil screening levels. In contrast, biochar amendment can be used to immobilize PFAS and mitigate key exposure risks at sites where phytoremediation alone cannot meet soil thresholds and there is a clear risk of groundwater contamination.

Our modeling shows that PFAS concentrations in agricultural soils can potentially be reduced to below current risk-based thresholds for agricultural soils in the U.S. within decade scales in most regions (Fig.1a). However, soil chemistry plays a critical role in remediation rates. Managing soil pH through enhanced weathering accelerated PFOS decline by 20–40%, cutting remediation timelines by more than a decade at typical contamination levels. This effect is less pronounced for PFOA (Fig 1b). However, for PFOS, one of the compounds of primary regulatory concern, our modeling strongly suggests that pH management substantially improves outcomes (Fig.1a).

The remediation process is governed by the soil–water partitioning behavior of PFAS, often described by the distribution coefficient (K_d). Importantly, K_d values are inversely correlated with plant uptake(*19*). When K_d values are lower, PFOS remain more mobile and bioavailable to plants(*18*, *19*). This relationship can be deliberately manipulated. Raising soil pH lowers K_d, thereby enhancing plant uptake and accelerating phytoremediation (Fig. 1a). In contrast, adding treatment-derived biochar increases K_d through strong PFOS sorption, suppressing plant uptake while substantially reducing the risk of leaching to groundwater. Although this decreases

phytoextraction, it is advantageous when groundwater protection is the primary concern. In practice, the approach can be tuned to balance retention and uptake depending on site-specific management priorities.

Through phytoremediation, PFOS concentrations in soil exponentially decline as hyperaccumulating crops (e.g., hemp and perennial grasses) draw down the contaminant pool. Harvested biomass converted to biochar and reapplied to the field can also serve to immobilize residual PFAS, thereby reducing their transfer into forage crops. This biochar pathway is particularly valuable at highly contaminated sites (> 100 ppb PFOS). Under scenarios with elevated contamination (e.g., the highest 90th percentile of sites) the combination of phytoremediation and transition to biochar addition reduced forage crop concentrations below conservative food-chain thresholds(*27*) within a decade—an outcome not achievable with phytoremediation alone (SI Section 1.6-1.9). At sites with lower pollution levels, it may be more effective to not add biochar such that higher rates of PFAS phytoremediation can be sustained until remediation below critical levels is complete. These results demonstrate that agricultural soils can be shifted from PFAS reservoirs into actively managed systems with reduced long-term risk. In addition, unlike traditional PFAS remediation approaches, this strategy empowers the communities most impacted by contamination—farmers—to directly remediate their land while potentially maintaining productive use.

We estimate that between 0.6 and 2.4 million hectares of U.S. cropland have been impacted by PFAS over the past five decades (SI Fig S3-S5), with a likely median value of roughly 1 million hectares. This estimate is conservative, as it excludes applications prior to 1976 and does not account for additional inputs such as wastewater effluent irrigation(*10*, *28*), paper mill sludge(*29*), or PFAS-containing pesticides(*30*, *31*). We estimate a mean soil burden of ~70 ng g^{-1} $\sum_{21}$ PFAS, with PFOS emerging as the dominant compound (average 35 ng g^{-1}). These levels are

consistent with reported ranges at biosolids-impacted sites globally and exceed proposed regulatory thresholds in several U.S. states(*14*, *32*, *33*), making PFOS the primary constraint on safe agricultural use on millions of arable acres. Without adoption of remediation strategies such as the one proposed here, PFAS impacted land will continue to pose risks to food security, ecosystem health, and groundwater quality.

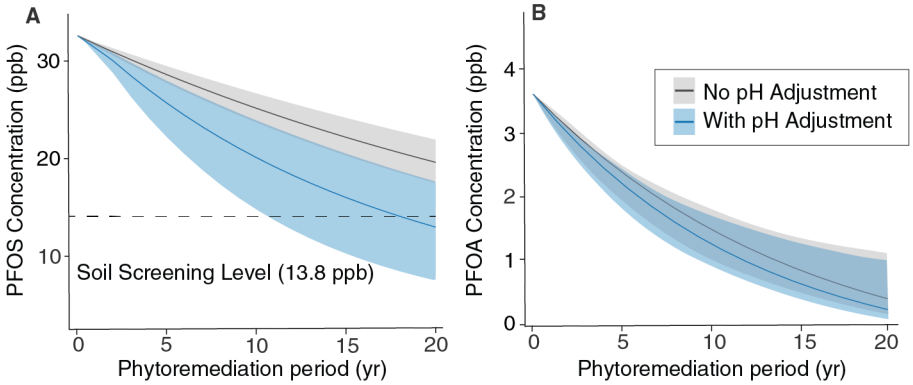

Fig. 1. Modeled PFOS and PFOA concentrations in soil under proposed remediation strategy. Modeled trajectories of plant-driven PFOS and PFOA removal in soils with and without a pH amendment. (a) PFOS concentrations in soil with the relevant agricultural screening level (14) and (b) PFOA concentrations in soil. In each panel, the solid line represents the modeled outcome under average site conditions, and the shaded region denotes the 95% confidence interval.

Carbon dioxide removal potential

The remediation strategy for PFAS-contaminated agricultural soils proposed here offers both an approach toward pollution management and a meaningful contribution to climate mitigation. We estimate a combined median national carbon dioxide removal (CDR) potential in the U.S. of ~10.8 Mt CO_2 yr^{-1} through this approach, with enhanced weathering contributing ~1.0 ± 0.3 Mt CO_2 yr^{-1} and biochar production ~9.8 Mt ± 3.5 CO_2 yr^{-1} (Fig 2.), with the main driver of uncertainty being the total amount of PFAS impacted land this strategy could be deployed on. To place this in context, U.S. CDR targets for achieving net-zero by 2050 are on the order of 0.2 Gt CO_2 yr^{-1} (*34*, *35*); thus, adoption of this strategy could achieve approximately 4-6% of the

national goal. Over a 20-year remediation period, this equates to roughly 220 Mt CO_2 removed. By contrast, conventional remediation strategies such as landfilling or thermal treatment of the top 30 cm of soil generate substantial CO_2 emissions, ranging from 92–800 tCO_2 ha^{-1} and totaling 110–960 $MtCO_2$ across the same land area over the same timeframe (see SI Fig S7).

Enhanced weathering estimates are based on applying finely ground basalt until soils reach a target pH of 7, using a reactive transport model designed to mimic weathering in croplands (*36*, *37*). We assume an 80% effective efficiency from the model estimates, reflecting ~10% loss of alkalinity during river–ocean transport, and ~10% life cycle and logistics emissions (see SI Section 1.10-1.11). Basalt was selected for its favorable CDR potential, nutrient content, and relatively low heavy metal risk. However, limestone may be more favorable in some regions and can also drive carbon removal(*38*). Biochar-derived carbon removal was estimated over the same ~1.2 million hectares of PFAS-impacted farmland, incorporating stochastic variation in biomass yields, pyrolyzer efficiency, and carbon content, and applying a ~10% deduction for life-cycle inefficiencies (SI Section 1.12). The resulting national median estimate was ~9.8 Mt CO_2 yr^{-1}, with the greatest contributions from California, Illinois, and Texas owing to their extensive contaminated cropland (Fig. 2A). Although additional region-specific LCAs are needed, these results provide an initial framework for evaluating the feasibility and climate co-benefits of this remediation pathway.

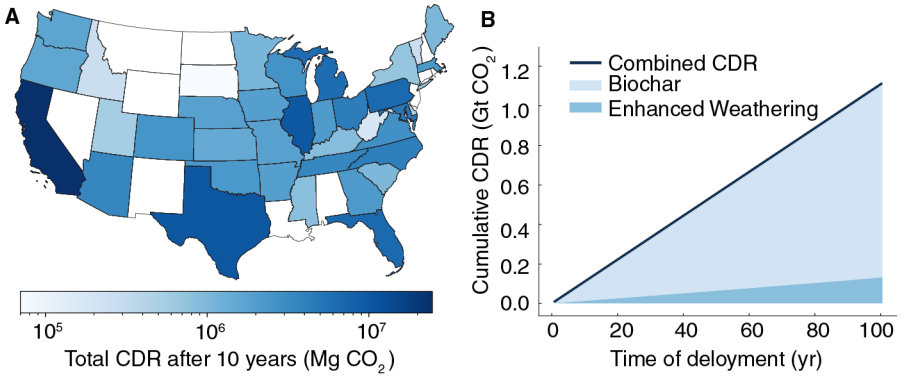

Fig 2. CDR potential from biochar and EW on PFAS-impacted farmland in the U.S. a) State-level CDR potential across impacted agricultural areas. b) Cumulative national CDR over time showing contributions from biochar and EW.

Economic feasibility

The proposed phytoremediation–biochar–enhanced weathering system delivers PFAS remediation at far lower cost than conventional technologies. Without carbon crediting, an estimated conservative mean remediation cost using this approach is approximately 4,000 ± 650 USD ha^{-1} yr^{-1} (SI sections 1.14 -1.16), with the main driver of cost being the transport and pyrolysis of harvested biomass (SI Fig S9). However, incorporating a social cost of carbon (SCC) of 190 USD tCO_2^{-1} offsets roughly 70% of this total, reducing net remediation expenditures to ~1,260 ± 700 USD ha^{-1} yr^{-1}**.**

Beyond the base cost of deploying this strategy we also assume a farmer incentive of 300–500 USD ha^{-1} yr^{-1}, based on approximate averages of net cash farm income for U.S. crop production businesses(*39*). This would allow for maintaining agricultural productivity and provide farmers with a stable income stream. If CDR were valued at 275 USD tCO_2^{-1}, within the range for current durable carbon credits (*40*, *41*), carbon revenues would fully cover all remediation costs (SI Fig S10). These SCC values are consistent with recent economic analyses, which place the social cost of carbon in the ~190–300 USD tCO_2^{-1} range(*41*). Taken together, our analysis suggests that this coupling of PFAS removal with durable carbon sequestration could enable a financially viable pathway to remediate contaminated farmland while simultaneously contributing to national climate-mitigation efforts.

By contrast, conventional soil remediation methods remain prohibitively expensive. Thermal treatment and excavation with off-site disposal cost an estimated 1.1 to 1.9 million USD per hectare, which is substantially higher than the estimated 25,000 USD per hectare for our strategy over a 20-year remediation period. Applied across the approximately 1.2 million hectares of

PFAS-contaminated farmland, these conventional approaches would translate to a total cost of 1.3 to 2.4 trillion USD (SI Fig. S11). In addition to the financial burden, which is 30 to 70 times higher than our proposed system, these approaches also permanently remove agricultural land from productive use, creating further economic stress for affected communities as they are forced to transition their land away from agriculture.

Biochar costs were parameterized using models adapted from the pyrolysis of dedicated biomass, with median production costs of 133 USD tCO_2^{-1} for large centralized facilities and 176 USD tCO_2^{-1} for mobile units (Fig. S9). Given the higher cost of mobile systems, only centralized configurations were included in our baseline analysis. ERW deployment costs were taken from established literature estimates of approximately 160 USD tCO_2^{-1} (*42*). However, the dominant cost driver for this system is the production and management of hemp and fescue biomass, which determines both phytoremediation capacity and the quantity of material requiring processing. This component also has the greatest potential for cost reduction through selective breeding, genetic modification, and the discovery of new hyperaccumulator species such as the recent *Oenothera rosea*, which exhibits PFOS remediation rates nearly twice those of the hemp used here (*43*, *44*). If commercialized and deployed at scale, such improved phytoremediators could substantially accelerate PFAS extraction and reduce total system costs.

The combined thermal and phyto-remediation strategy proposed here leverages existing agricultural infrastructure, equipment, and labor rather than the limited capacity and transport of soil burners or excavation equipment, a large reason for the stark reduction in cost. As a result, deployment could be brought to scale relatively rapidly. Importantly, this approach provides landowners with autonomy over the remediation process, in many cases enabling them to farm their land in a relatively familiar way while preserving agricultural value, generating a potential income stream, and allowing eventual transition back to traditional cash crop production.

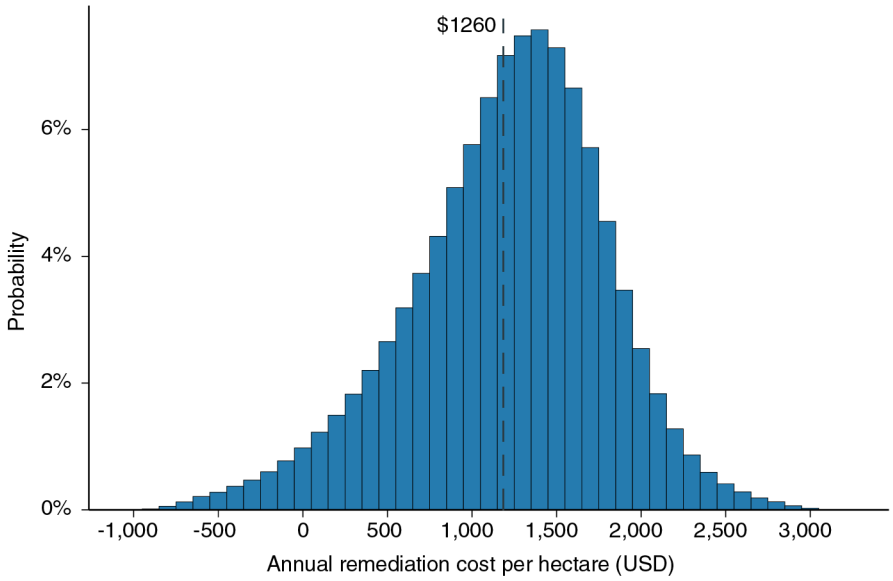

Fig. 3. Distribution of annual remediation costs.
Histogram shows the distribution of annual remediation costs generated by sampling biomass production costs, carbon removal rates, credit prices at $190 USD, treatment costs, and farmer income offsets from their empirical ranges. The dashed line indicates the median annual remediation cost.

Conclusion

PFAS contamination of agricultural soils represents a pervasive and persistent environmental challenge, with legacy biosolids applications having impacted millions of hectares of U.S. farmland and farms worldwide. In the U.S. soil PFAS concentrations frequently exceed proposed regulatory thresholds and limits for safe agricultural use. Current remediation methods, including thermal destruction and excavation with landfilling, are economically and logistically infeasible at scale, threatening farmland productivity while generating hundreds of millions of tons of CO_2 emissions.

We propose a remediation strategy combining phytoremediation, biochar production, and enhanced weathering. Our initial feasibility analysis indicates that this pathway could offer a scalable, cost-effective alternative to traditional soil remediation pathways. Soil pH management accelerates PFOS removal, cutting remediation timelines by more than a decade at typical

contamination levels. At sites with particularly high contamination, biochar immobilization reduces leaching to groundwater by more than 95% and can bring agricultural plant concentration to below agricultural risk thresholds within roughly a decade in the vast majority of sites. This dual approach allows flexibility on how each site is managed depending on site characteristics. The approach also provides significant carbon benefits—potentially providing 4–6% of U.S. CDR targets in 2050 for 1.5ºC of warming (*35*), demonstrating the dual environmental benefits of soil remediation and durable carbon removal. Economically, the strategy reduces remediation costs by over an order of magnitude relative to conventional methods, providing the lowest proposed methods deal with PFAS contamination in croplands.

Although this analysis is centered on U.S. cropland, PFAS contamination from biosolid application is a global issue. In Europe, approximately 50% of the 10 million tons of dry sewage sludge generated annually is applied to agricultural land(*45*), with the U.K. spreading ~70% (~1 million tons) of its biosolids(*46*). China applies ~5 million dry tons of biosolids to soils each year(*47*), while in Australia, 79.3% of the 372,000 tons produced in 2023 were used in agriculture(*48*). Given the persistent PFAS content in these materials, the remediation framework presented here is broadly applicable, providing a model for sustainable PFAS management worldwide.

References and Notes

1. M. G. Evich, M. J. B. Davis, J. P. McCord, B. Acrey, J. A. Awkerman, D. R. U. Knappe, A. B. Lindstrom, T. F. Speth, C. Tebes-Stevens, M. J. Strynar, Z. Wang, E. J. Weber, W. M. Henderson, J. W. Washington, Per- and polyfluoroalkyl substances in the environment. *Science* **375**, eabg9065 (2022).

2. D. Ackerman Grunfeld, D. Gilbert, J. Hou, A. M. Jones, M. J. Lee, T. C. G. Kibbey, D. M. O'Carroll, Underestimated burden of per- and polyfluoroalkyl substances in global surface waters and groundwaters. *Nat. Geosci.* **17**, 340–346 (2024).

3. B. Göckener, T. Weber, H. Rüdel, M. Bücking, M. Kolossa-Gehring, Human biomonitoring of per- and polyfluoroalkyl substances in German blood plasma samples from 1982 to 2019. *Environ. Int.* **145**, 106123 (2020).

4. CDC, Fast Facts: PFAS in the U.S. Population, *Per- and Polyfluoroalkyl Substances (PFAS) and Your Health* (2024). https://www.atsdr.cdc.gov/pfas/data-research/facts-stats/index.html.

5. C. L. Mitchell, J. Hollister, J. M. Fisher, S. C. Beitel, F. Ramadan, S. O'Leary, Z. T. Fan, K. Lutrick, J. L. Burgess, K. D. Ellingson, Differences in serum concentrations of per-and polyfluoroalkyl substances by occupation among firefighters, other first responders, healthcare workers, and other essential workers in Arizona, 2020–2023. *J. Expo. Sci. Environ. Epidemiol.* **35**, 437–444 (2025).

6. S. E. Fenton, A. Ducatman, A. Boobis, J. C. DeWitt, C. Lau, C. Ng, J. S. Smith, S. M. Roberts, Per- and Polyfluoroalkyl Substance Toxicity and Human Health Review: Current State of Knowledge and Strategies for Informing Future Research. *Environ. Toxicol. Chem.* **40**, 606–630 (2021).

7. E. M. Sunderland, X. C. Hu, C. Dassuncao, A. K. Tokranov, C. C. Wagner, J. G. Allen, A Review of the Pathways of Human Exposure to Poly- and Perfluoroalkyl Substances (PFASs) and Present Understanding of Health Effects. *J. Expo. Sci. Environ. Epidemiol.* **29**, 131–147 (2019).

8. L. G. Peter, L. S. Lee, Sources and Pathways of PFAS Occurrence in Water Sources: Relative Contribution of Land-Applied Biosolids in an Agricultural Dominated Watershed. *Environ. Sci. Technol.* **59**, 1344–1353 (2025).

9. M. A. Holly, K. M. Gunn, D. Keymer, J. R. Sanford, Evaluation of Per- and Polyfluoroalkyl Substances Leaching from Biosolids and Mitigation Potential of Biochar through Undisturbed Soil Columns. *ACS EST Water* **4**, 413–426 (2024).

10. Bothfeld, F, C. Mathieu, "PFAS Concentrations in Influent, Effluent, Solids, and Biosolids of Three Wastewater Treatment Plants" (22-03–028, Washington State Department of Ecology, 2022); https://apps.ecology.wa.gov/publications/documents/2203028.pdf.

11. EGLE, Initiatives to Evaluate the Presence of PFAS in Municipal Wastewater and Associated Residuals (Sludge/Biosolids) in Michigan. (2020).

12. A. K. Venkatesan, R. U. Halden, National inventory of perfluoroalkyl substances in archived U.S. biosolids from the 2001 EPA National Sewage Sludge Survey. *J. Hazard. Mater.* **252–253**, 413–418 (2013).

13. S. Greene, T. Phillips, T. Richman, L. Weber, D. Tobias, T. Lilly, A. Lutes, R. Warrier, B. Jacobs, A. Jarvis, J. Justice, C. Lindberg, J. Oliver, M. Brooks, M. Evich, R. Hermann, N. Birchfield, J. Mills, A. Adegbule, M. Card, D. Young, "DRAFT SEWAGE SLUDGE RISK ASSESSMENT FOR PERFLUOROOCTANOIC ACID (PFOA) CASRN 335-67-1 AND PERFLUOROOCTANE SULFONIC ACID (PFOS) CASRN 1763-23-1" (2025); https://www.epa.gov/system/files/documents/2025-01/draft-sewage-sludge-risk-assessment-pfoa-pfos.pdfhttps://www.epa.gov/system/files/documents/2025-01/draft-sewage-sludge-risk-assessment-pfoa-pfos.pdf.

14. Maine DEP, Maine PFAS Screening Levels (2023). https://www.maine.gov/dep/spills/topics/pfas/Maine%20PFAS%20Screening%20Levels_Rev_12_4_23.pdf.

15. Maine DEP, PFAS in Maine Response - Bureau of Agriculture, Food and Rural Resources: Maine DACF (2024). https://www.maine.gov/dacf/ag/pfas/pfas-response.shtml#dacf.

16. United States Chamber of Commerce, "PFOS and PFOA Private Cleanup Costs at Superfund Sites" (2022); https://www.uschamber.com/assets/documents/PFOS-and-PFOA-Private-Cleanup-Costs-at-Superfund-Sites-6.8.22.pdf.

17. Marc Mills, PFAS Treatment in Biosolids – State of the Science (2020). https://www.epa.gov/sites/default/files/2020-10/documents/r1-pfas_webinar_day_2_session_6_mills_final.pdf.

18. H. Campos-Pereira, Dan B. Kleja, L. Ahrens, A. Enell, J. Kikuchi, M. Pettersson, J. P. Gustafsson, Effect of pH, surface charge and soil properties on the solid–solution partitioning of perfluoroalkyl substances (PFASs) in a wide range of temperate soils. *Chemosphere* **321**, 138133 (2023).

19. E. R. Knight, J. Bräunig, L. J. Janik, D. A. Navarro, R. S. Kookana, J. F. Mueller, M. J. McLaughlin, An investigation into the long-term binding and uptake of PFOS, PFOA and PFHxS in soil – plant systems. *J. Hazard. Mater.* **404**, 124065 (2021).

20. F. Wang, X. Lu, X. Li, K. Shih, Effectiveness and Mechanisms of Defluorination of Perfluorinated Alkyl Substances by Calcium Compounds during Waste Thermal Treatment. *Environ. Sci. Technol.* **49**, 5672–5680 (2015).

21. R. DiStefano, T. Feliciano, R. A. Mimna, A. M. Redding, J. Matthis, Thermal destruction of PFAS during full-scale reactivation of PFAS-laden granular activated carbon. *Remediat. J.* **32**, 231–238 (2022).

22. L. J. Winchell, J. Cullen, J. J. Ross, A. Seidel, M. L. Romero, F. Kakar, E. Bronstad, M. J. M. Wells, N. B. Klinghoffer, F. Berruti, A. Miot, K. Y. Bell, Fate of biosolids-bound PFAS through pyrolysis coupled with thermal oxidation for air emissions control. *Water Environ. Res.* **96**, e11149 (2024).

23. E. Sørmo, L. Silvani, N. Bjerkli, N. Hagemann, A. R. Zimmerman, S. E. Hale, C. B. Hansen, T. Hartnik, G. Cornelissen, Stabilization of PFAS-contaminated soil with activated biochar. *Sci. Total Environ.* **763**, 144034 (2021).

24. A. K. Ilango, W. Zhang, Y. Liang, Uptake of per- and polyfluoroalkyl substances by Conservation Reserve Program's seed mix in biosolids-amended soil. *Environ. Pollut.* **363**, 125235 (2024).

25. D. Woolf, J. E. Amonette, F. A. Street-Perrott, J. Lehmann, S. Joseph, Sustainable biochar to mitigate global climate change. *Nat. Commun.* **1**, 56 (2010).

26. D. J. Beerling, E. P. Kantzas, M. R. Lomas, L. L. Taylor, S. Zhang, Y. Kanzaki, R. M. Eufrasio, P. Renforth, J.-F. Mecure, H. Pollitt, P. B. Holden, N. R. Edwards, L. Koh, D. Z. Epihov, A. Wolf, J. E. Hansen, S. A. Banwart, N. F. Pidgeon, C. T. Reinhard, N. J. Planavsky, M. Val Martin, Transforming US agriculture for carbon removal with enhanced weathering. *Nature* **638**, 425–434 (2025).

27. Maine CDC, Derivation of Action Levels for PFOS in Cows Milk (2017). https://www.maine.gov/dep/spills/topics/pfas/Derivation-of-Action-Levels-for-PFOS-in-Cows-Milk-03.28.17.pdf.

28. USDA, Use of recycled and reclaimed water sources for irrigation varies across the United States (2018). https://www.ers.usda.gov/data-products/charts-of-note/chart-detail?chartId=106153.

29. T. Turner, R. Wheeler, I. W. Oliver, Evaluating land application of pulp and paper mill sludge: A review. *J. Environ. Manage.* **317**, 115439 (2022).

30. N. Donley, C. Cox, K. Bennett, A. M. Temkin, D. Q. Andrews, O. V. Naidenko, Forever Pesticides: A Growing Source of PFAS Contamination in the Environment. *Environ. Health Perspect.* **132**, 075003 (2024).

31. A. Libenson, S. Karasaki, L. J. Cushing, T. Tran, J. L. Rempel, R. Morello-Frosch, C. E. Pace, PFAS-Contaminated Pesticides Applied near Public Supply Wells Disproportionately Impact Communities of Color in California. *ACS EST Water* **4**, 2495–2503 (2024).

32. O. US EPA, Regional Screening Levels (RSLs) - Generic Tables (2023). https://www.epa.gov/risk/regional-screening-levels-rsls-generic-tables.

33. FDEP, Provisional PFOA and PFOS Cleanup Target Levels & Screening Levels | Florida Department of Environmental Protection (2025). https://floridadep.gov/waste/district-business-support/documents/provisional-pfoa-and-pfos-cleanup-target-levels-screening.

34. A. Grubler, C. Wilson, N. Bento, B. Boza-Kiss, V. Krey, D. L. McCollum, N. D. Rao, K. Riahi, J. Rogelj, S. De Stercke, J. Cullen, S. Frank, O. Fricko, F. Guo, M. Gidden, P. Havlík, D. Huppmann, G. Kiesewetter, P. Rafaj, W. Schoepp, H. Valin, A low energy demand scenario for meeting the 1.5 °C target and sustainable development goals without negative emission technologies. *Nat. Energy* **3**, 515–527 (2018).

35. J. Kerry, The Long-Term Strategy of the United States, Pathways to Net-Zero Greenhouse Gas Emissions by 2050. (2021).

36. Y. Kanzaki, I. Chiaravalloti, S. Zhang, N. J. Planavsky, C. T. Reinhard, In silico calculation of soil pH by SCEPTER v1.0. *Geosci. Model Dev.* **17**, 4515–4532 (2024).

37. Y. Kanzaki, S. Zhang, N. J. Planavsky, C. T. Reinhard, Soil Cycles of Elements simulator for Predicting TERrestrial regulation of greenhouse gases: SCEPTER v0.9. *Geosci. Model Dev.* **15**, 4959–4990 (2022).

38. P. Raymond, N. Planavsky, C. T. Reinhard, Using carbonates for carbon removal. *Nat. Water* **3**, 844–847 (2025).

39. USDA, Farm Sector Income & Finances - Farm Business Income | Economic Research Service (2022). https://www.ers.usda.gov/topics/farm-economy/farm-sector-income-finances/farm-business-income?utmcom.

40. CDR.fyi, Current Market Prices (2024). https://www.cdr.fyi/.

41. U.S. EPA, Draft of Report on the Social Cost of Greenhouse Gases: Estimates Incorporating Recent Scientific Advances. (2022).

42. D. J. Beerling, E. P. Kantzas, M. R. Lomas, P. Wade, R. M. Eufrasio, P. Renforth, B. Sarkar, M. G. Andrews, R. H. James, C. R. Pearce, J.-F. Mercure, H. Pollitt, P. B. Holden, N. R. Edwards, M. Khanna, L. Koh, S. Quegan, N. F. Pidgeon, I. A. Janssens, J. Hansen, S. A. Banwart, Potential for large-scale CO2 removal via enhanced rock weathering with croplands. *Nature* **583**, 242–248 (2020).

43. X. Guo, X. Zhang, J. Chen, W. Shan, R. Wang, K. Wang, Z. Chen, L. Wang, Y. Zhang, Identification of a PFAS hyperaccumulator and elucidation of its translocation mechanism for sustainable phytoremediation. *Nat. Commun.* **16**, 10283 (2025).

44. W. Nassazzi, T.-C. Wu, J. Jass, F. Y. Lai, L. Ahrens, Phytoextraction of per- and polyfluoroalkyl substances (PFAS) and the influence of supplements on the performance of short–rotation crops. *Environ. Pollut.* **333**, 122038 (2023).

45. M. C. Collivignarelli, A. Abbà, A. Frattarola, M. Carnevale Miino, S. Padovani, I. Katsoyiannis, V. Torretta, Legislation for the Reuse of Biosolids on Agricultural Land in Europe: Overview. *Sustainability* **11**, 6015 (2019).

46. Biosolids Assurance Scheme, Biosolids Ag Good Practice Guidance (2019). https://assuredbiosolids.co.uk/wp-content/uploads/2019/01/Biosolids-Agric-Good-Practice-Guidance-January-2019.pdf.

47. X. Zhang, T. Zha, J. Zhu, X. Guo, Y. Liu, X. Zhang, T. Zha, J. Zhu, X. Guo, Y. Liu, Loading Capacity of Sewage Sludge for Forestry Application in Chinese Provincial Capital Cities. *Sustainability* **12** (2020).

48. P. Darvodelsky, Biosolids Production and End Use Survey – Australia 2022/23. (2023).

49. N. Beecher, Greg, Kester, Nora, Goldstein, Maile Lono-Batura, Juliana, Beecher, Janine, Burke-Wells, B. Toffey, National Summary, *National Biosolids Data State Summaries* (2022). https://www.biosolidsdata.org/national-summary.

50. G. Munoz, A. M. Michaud, M. Liu, S. Vo Duy, D. Montenach, C. Resseguier, F. Watteau, V. Sappin-Didier, F. Feder, T. Morvan, S. Houot, M. Desrosiers, J. Liu, S. Sauvé, Target and Nontarget Screening of PFAS in Biosolids, Composts, and Other Organic Waste Products for Land Application in France. *Environ. Sci. Technol.*, doi: 10.1021/acs.est.1c03697 (2021).

51. O. US EPA, Basic Information about Sewage Sludge and Biosolids (2024). https://www.epa.gov/biosolids/basic-information-about-sewage-sludge-and-biosolids.

52. N. Beecher, Greg, Kester, Nora, Goldstein, Maile Lono-Batura, Juliana, Beecher, Janine, Burke-Wells, B. Toffey, State Summaries, *National Biosolids Data State Summaries* (2022). https://www.biosolidsdata.org/state-summaries.

53. S. G. Hughes, “PFAS in Biosolids: A Review of State Efforts & Opportunities for Action” (2023).

54. G. R. Johnson, PFAS in soil and groundwater following historical land application of biosolids. *Water Res.* **211**, 118035 (2022).

55. U.S. EPA, “Biosolids Technology Fact Sheet: Land Application of Biosolids” (EPA 832-F-00-064, Office of Water, Washington, DC, 2000); https://www.epa.gov/sites/default/files/2018-11/documents/land-application-biosolids-factsheet.pdf.

56. Maine DEP, Maine DEP PFAS Investigation (Formerly the “Septage and Sludge Map”) (2024). https://maine.maps.arcgis.com/apps/webappviewer/index.html?id=468a9f7ddcd54309bc1ae8ba173965c7.

57. USDA, Farms and Land in Farms 2024 Summary. (2024).

58. Richard Becker, Allan R. Wilks, raw Geographical Maps, version R package version 3.4.2 (2023); https://CRAN.R-project.org/package=maps.

59. U. N. H. S. Programme, *Global Atlas of Excreta, Wastewater Sludge, and Biosolids Management: Moving Forward the Sustainable and Welcome Uses of a Global Resource* (UN-HABITAT, 2009).

60. U.S. Census Bureau., Gazetteer Files - State, (2021); https://www.census.gov/geographies/reference-files/time-series/geo/gazetteer-files.html.

61. X. Chen, L. Zhu, X. Pan, S. Fang, Y. Zhang, L. Yang, Isomeric specific partitioning behaviors of perfluoroalkyl substances in water dissolved phase, suspended particulate matters and sediments in Liao River Basin and Taihu Lake, China. *Water Res.* **80**, 235–244 (2015).

62. R. Hunter Anderson, D. T. Adamson, H. F. Stroo, Partitioning of poly- and perfluoroalkyl substances from soil to groundwater within aqueous film-forming foam source zones. *J. Contam. Hydrol.* **220**, 59–65 (2019).

63. C. P. Higgins, R. G. Luthy, Sorption of Perfluorinated Surfactants on Sediments. *Environ. Sci. Technol.* **40**, 7251–7256 (2006).

64. I. Ross, J. McDonough, J. Miles, P. Storch, P. T. Kochunarayanan, E. Kalve, J. Hurst, S. S. Dasgupta, J. Burdick, A review of emerging technologies for remediation of PFASs. *Remediat. J.* **28**, 101–126 (2018).

65. D. K. Huff, L. A. Morris, L. Sutter, J. Costanza, K. D. Pennell, Accumulation of six PFAS compounds by woody and herbaceous plants: potential for phytoextraction. *Int. J. Phytoremediation* **22**, 1538–1550 (2020).

66. Sumit Sharma, Jason Warren, Basics of Soil Bulk Density - Oklahoma State University (2024). https://extension.okstate.edu/fact-sheets/basics-of-soil-bulk-density.html.

67. E. Sørmo, C. B. M. Lade, J. Zhang, A. G. Asimakopoulos, G. W. Åsli, M. Hubert, A. I. Goranov, H. P. H. Arp, G. Cornelissen, Stabilization of PFAS-contaminated soil with sewage sludge- and wood-based biochar sorbents. *Sci. Total Environ.* **922**, 170971 (2024).

68. I. Battisti, A. R. Trentin, A. Sabia, A. Masi, G. Renella, Soil Amendment with Biochar Reduces the Uptake and Translocation of Perfluoroalkyl Substances by Horticultural Plants Grown in a Polluted Area. Social Science Research Network 4944118 [Preprint] (2024). https://doi.org/10.2139/ssrn.4944118.

69. W. Zhang, Y. Liang, Changing bioavailability of per- and polyfluoroalkyl substances (PFAS) to plant in biosolids amended soil through stabilization or mobilization. *Environ. Pollut.* **308**, 119724 (2022).

70. Maine DACF, Assessing PFAS Contamination and Managing Risks on Dairy Farms in Maine. (2022).

71. Y. Kanzaki, N. J. Planavsky, S. Zhang, J. Jordan, T. J. Suhrhoff, C. T. Reinhard, Soil cation storage is a key control on the carbon removal dynamics of enhanced weathering. *Environ. Res. Lett.* **20**, 074055 (2025).

72. S. Adhikari, E. Moon, J. Paz-Ferreiro, W. Timms, Comparative analysis of biochar carbon stability methods and implications for carbon credits. *Sci. Total Environ.* **914**, 169607 (2024).

73. City of Fort Collins Water Reclamation, Biosolids Management Performance Report (2017). https://www.fcgov.com/utilities/img/site_specific/uploads/jw_09112018_biosolids-management-program-annual-report.pdf?utm_source=chatgpt.com.

74. G. Liu, E. Hanlon, Soil pH Range for Optimum Commercial Vegetable Production: HS1207/HS1207, 10/2012. *EDIS* **2012** (2012).

75. USDA, Soil Organic Matter (2014). https://www.nrcs.usda.gov/sites/default/files/2022-10/Soil%20Organic%20Matter.pdf?utm.com.

76. USDA, USDA Unveils Updated Plant Hardiness Zone Map : USDA ARS (2023). https://www.ars.usda.gov/news-events/news/research-news/2023/usda-unveils-updated-plant-hardiness-zone-map/?utm_source=chatgpt.com.

77. B. Cantoni, A. Turolla, J. Wellmitz, A. S. Ruhl, M. Antonelli, Perfluoroalkyl substances (PFAS) adsorption in drinking water by granular activated carbon: Influence of activated carbon and PFAS characteristics. *Sci. Total Environ.* **795**, 148821 (2021).

78. E. Sørmo, L. Silvani, N. Bjerkli, N. Hagemann, A. R. Zimmerman, S. E. Hale, C. B. Hansen, T. Hartnik, G. Cornelissen, Stabilization of PFAS-contaminated soil with activated biochar. *Sci. Total Environ.* **763**, 144034 (2021).

79. H. N. P. Vo, T. M. H. Nguyen, H. H. Ngo, W. Guo, P. Shukla, Biochar sorption of perfluoroalkyl substances (PFASs) in aqueous film-forming foams-impacted groundwater: Effects of PFASs properties and groundwater chemistry. *Chemosphere* **286**, 131622 (2022).

80. M. Askeland, B. O. Clarke, S. A. Cheema, A. Mendez, G. Gasco, J. Paz-Ferreiro, Biochar sorption of PFOS, PFOA, PFHxS and PFHxA in two soils with contrasting texture. *Chemosphere* **249**, 126072 (2020).

81. H. Yoo, J. W. Washington, T. M. Jenkins, J. J. Ellington, Quantitative Determination of Perfluorochemicals and Fluorotelomer Alcohols in Plants from Biosolid-Amended Fields using LC/MS/MS and GC/MS. *Environ. Sci. Technol.* **45**, 7985–7990 (2011).

82. S. P. Alesso, R. Tapias, J. Alaejos, M. Fernández, Biomass Yield and Economic, Energy and Carbon Balances of Ulmus pumila L., Robinia pseudoacacia L. and Populus × euroamericana (Dode) Guinier Short-Rotation Coppices on Degraded Lands under Mediterranean Climate. *Forests* **12**, 1337 (2021).

83. IPCC, Method for Estimating the Change in Mineral Soil Organic Carbon Stocks from Biochar Amendments (2019). https://www.ipcc-nggip.iges.or.jp/public/2019rf/pdf/4_Volume4/19R_V4_Ch02_Ap4_Biochar.pdf?utm_source=chatgpt.com.

84. NACFE, NACFE: Fleet Fuel Study, *NACFE* (2024). http://nacfe.org/research/affs/.

85. O. US EPA, Greenhouse Gas Emissions from a Typical Passenger Vehicle (2016). https://www.epa.gov/greenvehicles/greenhouse-gas-emissions-typical-passenger-vehicle.

86. U.S. DOT, Maximum Legal Vehicle Weight Limits (2024). https://www.dot.nh.gov/sites/g/files/ehbemt811/files/inline-documents/truck-weights.pdf.

87. R. Alvarez-Ruiz, L. S. Lee, Y. Choi, Fate of per- and polyfluoroalkyl substances at a 40-year dedicated municipal biosolids land disposal site. *Sci. Total Environ.* **954**, 176540 (2024).

88. Office of Rail and Road, Rail Emissions. https://dataportal.orr.gov.uk/media/1993/rail-emissions-2020-21.pdf?utm_source=chatgpt.com.

89. Vern Grubinger, Managing Nitrogen on Organic Farms (2005). https://www.uvm.edu/vtvegandberry/factsheets/managingNorganic.html?utm_source=chatgpt.com .

90. D. W. Pribyl, A critical review of the conventional SOC to SOM conversion factor. *Geoderma* **156**, 75–83 (2010).

91. A. J. Franzluebbers, Soil organic matter stratification ratio as an indicator of soil quality. *Soil Tillage Res.* **66**, 95–106 (2002).

92. US EPA, Incinerator and Cement Kiln Capacity For Hazardous Waste Treatment (1986). https://nepis.epa.gov/Exe/ZyNET.exe/2000TL9E.txt?ZyActionD=ZyDocument&Client=EPA&Index=1986%20Thru%201990&Docs=&Query=&Time=&EndTime=&SearchMethod=1&TocRestrict=n&Toc=&TocEntry=&QField=&QFieldYear=&QFieldMonth=&QFieldDay=&UseQField=&IntQFieldOp=0&ExtQFieldOp=0&XmlQuery=&File=D%3A%5CZYFILES%5CINDEX%20DATA%5C86THRU90%5CTXT%5C00000009%5C2000TL9E.txt&User=anonymous&Password=anonymous&SortMethod=h%7C-&MaximumDocuments=1&FuzzyDegree=0&ImageQuality=r75g8/r75g8/x150y150g16/i425&Display=hpfr&DefSeekPage=&SearchBack=ZyActionL&Back=ZyActionS&BackDesc=Results%20page&MaximumPages=1&ZyEntry=3.

93. S. A. Ishak, H. Hashim, Low carbon measures for cement plant – a review. *J. Clean. Prod.* **103**, 260–274 (2015).

94. IPCC, Emissions From Waste Incineration (2018). https://www.ipcc-nggip.iges.or.jp/public/gp/bgp/5_3_Waste_Incineration.pdf.

95. J. Han, C. Xu, J. Jin, J. Hu, PCNs, PCBs, and PCDD/Fs in Soil around a Cement Kiln Co-Processing Municipal Wastes in Northwestern China: Levels, Distribution, and Potential Human Health Risks. *Int. J. Environ. Res. Public. Health* **19**, 12860 (2022).

96. USDA, 2022 Census of Agriculture: Number of U.S. farms falls below 2 million | Economic Research Service (2022). https://www.ers.usda.gov/data-products/charts-of-note/chart-detail?chartId=108629.

97. F.-X. Collard, S. Wijeyekoon, P. Bennett, Commercial status of direct thermochemical liquefaction technologies.

98. ARTi - Pyrolysis Reactors, *ARTi* (2025). https://www.arti.com/reactors/.

99. CharBoss (2023). https://airburners.com/products/boss-series/charboss/.

100. F. Amalina, A. S. A. Razak, S. Krishnan, H. Sulaiman, A. W. Zularisam, M. Nasrullah, Biochar production techniques utilizing biomass waste-derived materials and environmental applications – A review. *J. Hazard. Mater. Adv.* **7**, 100134 (2022).

101. M. Coleman, D. Page-Dumroese, J. Archuleta, P. Badger, W. Chung, T. Venn, D. Loeffler, G. Jones, K. McElligott, Can portable pyrolysis units make biomass utilization affordable while using bio-char to enhance soil productivity and sequester carbon? *Jain Theresa B Graham Russell T Sandquist Jonathan Integr. Manag. Carbon Sequestration Biomass Util. Oppor. Chang. Clim. Proc. 2009 Natl. Silvic. Workshop 2009 June 15-18 Boise ID Proc. RMRS-P-61 Fort Collins CO US Dep. Agric. For. Serv. Rocky Mt. Res. Stn. P 159-168* **61**, 159–168 (2010).

102. C. Hellwinckel, D. Ugarte, J. Field, M. Langholtz, Chapter 5: Biomass from Agriculture, Oak Ridge National Laboratory (ORNL), Oak Ridge, TN (United States), Bioenergy Knowledge Discovery Framework (BEKDF) (2024); https://doi.org/10.23720/BT2023/2316171.

103. Hale, 10 Tips to Managing Semi-Truck Fuel Efficiency, *Hale Trailer Brake & Wheel* (2025). https://haletrailer.com/blog/semi-truck-fuel-efficiency/.

104. Fuel Economy of Heavy Duty Vehicles (1976). https://nepis.epa.gov/Exe/ZyNET.exe/9100UPS2.TXT?ZyActionD=ZyDocument&Client=EPA&Index=1976+Thru+1980&Docs=&Query=&Time=&EndTime=&SearchMethod=1&TocRestrict=n&Toc=&TocEntry=&QField=&QFieldYear=&QFieldMonth=&QFieldDay=&IntQFieldOp=0&ExtQFieldOp=0&XmlQuery=&File=D%3A%5Czyfiles%5CIndex%20Data%5C76thru80%5CTxt%5C00000019%5C9100UPS2.txt&User=ANONYMOUS&Password=anonymous&SortMethod=h%7C-&MaximumDocuments=1&FuzzyDegree=0&ImageQuality=r75g8/r75g8/x150y150g16/i425&Display=hpfr&DefSeekPage=x&SearchBack=ZyActionL&Back=ZyActionS&BackDesc=Results%20page&MaximumPages=1&ZyEntry=1&SeekPage=x&ZyPURL.

105. O. US EPA, Greenhouse Gas Emissions from a Typical Passenger Vehicle (2016). https://www.epa.gov/greenvehicles/greenhouse-gas-emissions-typical-passenger-vehicle.

106. US EIA, Gasoline and Diesel Fuel Update. https://www.eia.gov/petroleum/gasdiesel/index.php.

107. NH DOT, Transport Trucking Weight Limits (1992). https://www.dot.nh.gov/sites/g/files/ehbemt811/files/inline-documents/truck-weights.pdf.

108. Bureau of Transportation Statistics, National Transportation Statistics (NTS). Bureau of Transportation Statistics [Preprint] (2019). https://doi.org/10.21949/1503663.

109. Eric A. DeVuyst, Roger Sahs, What is the Economic Cost of a Bale of Hay? - Oklahoma State University (2024). https://extension.okstate.edu/fact-sheets/what-is-the-economic-cost-of-a-bale-of-hay.html.

110. Chad Hart, 2025 Estimated Costs of Crop Production in Iowa. (2025).

111. John J. Hanchar, Economics of Producing Industrial Hemp in New York State: Projected Costs and Returns, 2019 Budgets (2019). https://bpb-us-e1.wpmucdn.com/blogs.cornell.edu/dist/a/7491/files/2017/04/HancharJohn-economics-of-industrial-hemp-2019-analysis-update-2019_01_22-28o6gqp.pdf?utm_source=chatgpt.com.

112. D. J. Beerling, D. Z. Epihov, I. B. Kantola, M. D. Masters, T. Reershemius, N. J. Planavsky, C. T. Reinhard, J. S. Jordan, S. J. Thorne, J. Weber, M. Val Martin, R. P. Freckleton, S. E. Hartley, R. H. James, C. R. Pearce, E. H. DeLucia, S. A. Banwart, Enhanced weathering in the US Corn Belt delivers carbon removal with agronomic benefits. *Proc. Natl. Acad. Sci.* **121**, e2319436121 (2024).

Acknowledgments:
The authors would like to thank Winslow and Laura Robinson of Fable Farmstead for their cooperation and support to conduct PFAS research on their land.

Funding:

Schmidt Family Foundation G-25-68435, NP, JT

Natural Environment Research Council (NERC) NE/S007210/1, MD

Author contributions:

Conceptualization: JTT, CK, NP, MD
Methodology: JTT, MD, YK, TJS
Investigation: JTT, MD, LB
Visualization: JTT, TJS, EM
Funding acquisition: JTT, NP, MD
Writing – original draft: JTT, NP, MD
Writing – review & editing: RJ, CTR, NP, TJS, CK

Diversity, equity, ethics, and inclusion [optional]: This work was conducted in alignment with Yale University's commitments to ethical research and inclusive collaboration. The project team represented multiple disciplines and career stages, and early-career researchers were actively mentored and involved in all phases of the study.

Competing interests: Authors declare that they have no competing interests

Data and materials availability: All data are available in the main text or the supplementary materials

Supplementary Materials

Materials and Methods

Figs. S1 to S11

Tables S1 to S9

References (*49-112*)

Supplementary Materials for

Integrated thermal and phyto-remediation of agricultural soils impacted by PFAS

Authors: Jake T Thompson[1], Millie Dobson[2], Tim Jesper Suhrhoff[3], Yoshiki Kanzaki[4], Chloe Kent[1], Lucinda Bryce[5], Rachel James[2], Ella Milliken[1], Christopher T Reinhard[4], Noah Planavsky[1]*

Affiliations:

[1]Department of Earth and Planetary Sciences, Yale University, 10 Whitney Ave., New Haven CT 06511 USA

[2]School of Ocean and Earth Science, National Oceanography Centre Southampton, University of Southampton Waterfront Campus, Southampton SO14 3ZH, UK

[3]Yale Center for Natural Carbon Capture, Yale University, New Haven, Connecticut 06511, USA

[4]School of Earth & Atmospheric Sciences, Georgia Institute of Technology, Atlanta, Georgia 30332, USA

[5]Department of Earth, Environmental, and Planetary Sciences, Brown University, Providence, Rhode Island 02912, USA

* corresponding author: noah.planavsky@yale.edu

Contents

1. Materials and Methods

Estimated mass of biosolids land applied in the U.S.

The mass of biosolids generated and land-applied in the U.S. was derived from two primary data sources: (1) a national inventory of biosolids generation and application (*17*) and (2) the National Biosolids Generation Project database, which contains state- and national-level inventories(*49*). These datasets provided national estimates of land-applied biosolids for the years 1976, 1984, 1988, 1998, 2004, 2010, and 2018.

To estimate the annual biosolids land application for years not explicitly reported, interpolation and extrapolation methods were applied. For years between recorded data points, the average of the two adjacent values was used as the estimated mass. For years prior to the earliest data point and post latest (e.g., 1975, 2019 and 2020) the last available datapoint was extrapolated. These values were compiled for the years 1975–2020 and summed to estimate the total mass of biosolids land-applied over this period. This range was selected based on historical evidence of PFAS in biosolids dating back to 1976(*50*) and the continued use of PFAS containing biosolids on agricultural land to the modern day(*51*).

Area of impacted land

The area of impacted agricultural land within the U.S. was estimated using standard land application rates based on literature accounts and state biosolid application recommendations (*52–54*). These rates ranged from 6.3 – 10.1 t hectare^{-1} year^{-1}.

$$B_h = \text{application rate} \times \text{duration of application} \quad (1)$$

With the average application rate being the same value used for EPA's draft biosolid risk assessment for PFOA and PFOS 7.6 t hectare^{-1} year^{-1}. These values fall within agronomic estimates conducted by EPA previously (2.5 – 11 t hectare^{-1} year^{-1}) (*55*). Where much of the

uncertainty comes from in this assessment is the lack of information on the amount of time biosolids were applied to land. Biosolid application permit records exist for many states however the length of time, application rate, and if biosolids were even added is rarely documented. For this assessment we have constrained the time of application to once per year for 7 to 20 years of application (parameters for all equations used in this section are in Table S1)

$$H_I = \frac{C_b}{B_h} \quad (2)$$

PFAS concentration and frequency

The concentrations of PFAS and the distribution of their detection frequency at an impacted agricultural site come from a relatively robust dataset (Maine DEPs PFAS state assessment)(*56*). At the time of this analysis this data contained ~800 datapoints for PFAS impacted sites. To refine the dataset for analysis, samples that were not categorized as “Sludge Utilization Sites” were excluded, as the dataset also included entries labeled as “Surface Spills” and “Septage Storage.” Additionally, any samples containing the terms “Landfill” or “Airport” were removed to ensure that the remaining data primarily reflected farmland biosolid applications (hereafter referred to as "Farm Data"). This filtering process resulted in the removal of approximately 200 samples from the dataset.

The remaining 563 sites contained data for total $\sum_{21}$ PFAS (PFBA, PFBS, PFDA, PFDoA, PFDS, PFHpA, PFHpS, PFHxA, PFHxDA, PFHxS, PFNA, PFNS, PFOA, PFODA, PFOS, PFOSA, PFPeA, PFPeS, PFTeA, PFTriA, and PFUnDA). The average concentration of $\sum_{21}$ PFAS and the frequency of detection at that concentration was recorded as well as the average concentration for each PFAS. The location and concentration of PFAS at these sites were plotted (Fig S1) and relative concentrations of $\sum_{21}$ PFAS across the sites (Fig S2).

Spatial Location of PFAS Impacted Land: State, Point, and Fraction of Agricultural Land

After determining the total amount of impacted land within the U.S., estimates were made to find the general distribution of this land across states. For these estimates two nationwide assessments detailing the amount of biosolids created for land application by each state were sourced (*49*, *52*). This data provided the ratio of biosolids produced by each state which was then multiplied by the total amount of impacted land within the U.S. to get an estimated amount of land within each state impacted by PFAS through biosolid application. This data was then used in comparison to a USDA database on the amount of agricultural land in farms for each state (*57*). The ratio of "land in farms" to the estimated median amount of impacted land in each state provided the data presented in Fig S3.

For CDR determinations, a higher resolution estimate of the amount of impacted land was needed. In this case the amount of impacted land from each state was divided into 1,000-hectare blocks rounded down. The blocks were then assigned a random coordinate within each states geometry provided by R's "maps" package(*58*). These points were then reselected within each state but weighted by population. This was done because wastewater treatment plant load and biosolids production are heavily influenced by population served and the cost benefit of using biosolids as an agricultural amendment is strongly impacted by transport distance(*59*). To spatially distribute these blocks within each state, latitude–longitude points were sampled with probabilities proportional to local population density coming from U.S. Census data (*60*). For each spatial unit *j* within state *i*, the selection weight was defined as:

$$Weighted\ Cordinates = \frac{D_{ij}}{\sum_j D_{ij}} \quad (3)$$

where *Dij* is the population density of unit *j*. Weighted random sampling was performed for each 1,000 hectare block generated per state, with replacement, to generate point coordinates

representing impacted areas. The resulting data for the 1,000 hectare plots is shown in the Fig S4 and the relative amount of agricultural land for each state in Fig S5.

Remediation site conditions

The site conditions from this this baseline theoretical site comes from special mapping data from Maine DEPs remediation program (*56*). To initialize year-zero site conditions for the model, we extracted soil pH values across Maine croplands using an empirical Bayesian kriging raster dataset (cite). These values were matched to field sample coordinates from known sludge-impacted sites. Each sample location was georeferenced and overlaid onto the raster, allowing soil pH to be spatially assigned to each site. This provided a realistic distribution of initial soil pH conditions used to simulate PFAS partitioning and remediation behavior in year zero of the model. For both soil pH and PFAS concentrations the median value across all sites (n=563) was selected.

For total organic carbon (TOC) and the fraction of organic carbon (f_{oc}), values were randomly assigned within a realistic range observed in northeastern agricultural soils. Specifically, foc was sampled from a uniform distribution between 0.01 and 0.03, and TOC was then calculated as 100 × f_{oc}. These values reflect typical soil organic carbon levels for surface horizons in cultivated areas of Maine. Since partitioning of PFAS to soil is driven in part by organic carbon content, this step was critical for estimating initial distribution coefficients (K_d) and aqueous concentrations (C_w) under year-zero conditions.

Modeling plant uptake efficiency based on Kd and pH change

To simulate PFAS uptake dynamics in plants across varying soil conditions, we constructed a modeling framework linking soil pH to PFAS sorption and subsequent plant removal efficiencies. Experimental data on PFAS sorption to soil organic fraction (K_{oc}) in high TOC soils

from Campos-Pereira et al. (2023) was used to develop compound-specific linear models describing log K_{oc} as a function of pH for PFOS and PFOA.

$$\log_{10}(K_{\mathrm{oc}}) = m \cdot \mathrm{pH} + b \tag{4}$$

Each model was fit using empirical pH-log K_{oc} relationships and then used to generate predicted K_{oc} values for each compound at target pH values (e.g., 5.5, the reported pH in pot trials from (Nassazzi et al. 2023). These log K_{oc} values were back-transformed and multiplied by simulated site-specific soil organic carbon fractions to calculate partition coefficients per compound per site.

Next, PFAS uptake efficiency was modeled as a function of K_d using exponential decay models fit to observed removal efficiencies in hemp (*44*). Reported removal efficiencies for perfluoroalkyl carboxylic acids (PFCAs) and perfluoroalkyl sulfonic acids (PFSAs) were correlated with their respective K_{oc}, which were either calculated using the Campos-Pereira pH-dependent K_{oc} models(*18*) or obtained from published literature (*61–63*) . Removal efficiency data and corresponding K_{oc} values from Nassazzi et al. 2023 (*44*) were compiled into a dataset and the exponential decay model of the form:

$$R_{\mathrm{plant}} = a \cdot \exp(-b \cdot K_{\mathrm{oc}}) \tag{5}$$

was fit to the data using nonlinear least squares regression to capture the relationship between removal efficiency in hemp and K_{oc} values. Log-transforming the removal efficiency allowed linear regression to estimate model parameters a and b, which characterize the exponential decay trend. Similarly, for PFSAs, removal efficiencies were modeled as a function of K_{oc} using the

same exponential approach. The distinction between PFCAs and PFSAs was made because they exhibit different sorption and plant uptake behaviors(*18*, *62*, *64*).

Phytoremediation

The phytoremediation scenario presented soil conditions and PFAS concentrations as described in the site conditions above. In short, these PFAS concentrations are the average values for the state assessment conducted in Maine for suspect PFAS impacted agricultural sites (n= 563). The presented remediation situation was selected as a realistic scenario where hemp is planted in the active growing season and harvested after ~120 days, that biomass is collected for pyrolysis and red fescue grass is planted (a cover crop shown to have high remediation potential(*65*)), next growing season the fescue is removed and bailed, and hemp is planted again to start the cycle over again.

The model simulates annual changes in PFOS and PFOA concentrations in soil based on evolving soil pH, organic carbon content, and predicted sorption behavior. Partitioning between soil and water was governed by predicted K_{oc}, which were estimated as a function of pH using a site-calibrated regression described above. These K_{oc} values were then used to compute distribution coefficients (K_d) and dissolved PFOS concentrations, assuming equilibrium sorption.

PFOS and PFOA removal by plants was modeled separately for hemp and red fescue. Red fescue removal was applied as a fixed percentage drawn with variability from published experimental values(*65*). Each year, the remaining soil PFOS concentration was calculated by applying the combined removal of both plant species, adjusted to ensure a minimum 0.5% annual reduction to avoid unrealistic model outcomes at very high K_{oc} values.

Simulations were run for 20 years under a Monte Carlo framework to capture uncertainty in key parameters including K_{oc} variability, annual pH change, and red fescue uptake efficiency. A

triangular distribution was used to simulate growing-season length to capture interannual variability in climate and crop growth duration. Plant uptake efficiency was scaled by the ratio of the modeled season length to the reference study's duration of 90 days (*44*). This was done so that empirical data used to predict removal rates were not limited to a 90 day growing cycle:

$$S_{hemp} = \frac{G_s}{G_{ref}} \quad (6)$$

$$R_{hemp,t} = f(K_{oc,t}) \cdot S_{hemp} \quad (7)$$

$$C_{soil,t} = C_{soil,t-1} \times (1 - R_{hemp}) \times (1 - R_{fescue}) \quad (8)$$

For the Monte Carlo analysis, 1,000 simulations were conducted by sampling from normal distributions for each uncertain parameter presented in Table S2. The model tracked PFOS and PFOA soil concentrations across all simulations, and outputs included the mean, 5th, and 95th percentile concentrations over time. A secondary scenario was also run in which K_{oc} was held constant (no pH effect) to isolate the impact of soil chemistry evolution.

Biochar Amendment and Sorption Coefficients

To evaluate the impact of biochar amendment on PFAS sorption, we modeled K_d dynamics over a 15-year period. The total soil mass per hectare was estimated as 3,900 tons, assuming a soil depth of 30 cm and a bulk density of 1,300 kg/m³ (*66*). To simulate the variability of PFAS sorption in amended soils, the model stochastically estimates the K_d using a combination of two components: (1) a probabilistic biochar-water coefficient (K_f) that is compound-specific, and (2) an adjustment factor based on the mass and effectiveness of biochar present in the soil.

The biochar sorption potential is represented by K_f, which is assumed to follow a normal distribution based on the range of values reported in the literature (*9*, *67*, *68*):

$$logK_f \sim \mathcal{N}\left(\log_{10}(\overline{K_f}), \sigma^2_{\log K_f}\right) \quad (9)$$

The estimated K_d for each iteration is then calculated by adjusting the stochastic K_f value with a biochar efficiency factor, which incorporates both the mass fraction of biochar in the soil and an efficiency correction designed to account for competitive sorption at lower biochar addition ranges (i.e., <1% biochar: soil). Table S3 summarizes the parameters used for these calculations. This comes from the literature on the effectiveness of biochar to limit plant uptake in amended soils (*9*, *24*, *69*). The effect typically seen is that biochar has a limited to no effect on the plant uptake until a threshold is reached, likely due to competitive sorption within the soil/ porewater. Table S4 summarizes the results of existing studies exploring applied sorbents impact on plant uptake and is the basic for this model. To account for this lag in plant uptake potential the biochar's effectiveness on limiting plant uptake was corrected until 1% biochar by mass of reached, a value shown to limit uptake of PFOS (*24*).

$$\text{biochar percent}_t = \left(\frac{\Sigma_{i=1}^{t} \text{Mass}_{\text{biochar},i}}{\text{Mass}_{\text{soil}}}\right) \times 100 \quad (10)$$

$$eff_b = \begin{cases} 0.5 \cdot \text{biochar}\%, & \text{if biochar}\% < 1 \\ 0.5 + (\text{biochar}\% - 1), & \text{if biochar}\% \geq 1 \end{cases} \quad (11)$$

The $eff_{biochar}$ coefficient then is used to determine the K_d at the site with the new addition of biochar:.

$$K_d = 10^{\log K_f} \times \left(\frac{\text{eff}_{\text{biochar}}}{100} \right) \quad (12)$$

The new Kd is then added to the soil Kd at year 0 or with no biochar addition which is 10 L/Kg for PFOA and 100 L/Kg for PFOS based on literature values(*63*). To avoid unrealistically high sorption values resulting from the tail of the log-normal distribution, the model imposes an upper cap on K_d denoted as K_{dmax}.

As established before in section 1.6 the removal of PFAS via plant uptake was assumed to be inversely related to its sorption (i.e., compounds with lower sorption K_d remain more available in the soil solution and are more likely to be taken up by plants).To capture this relationship, we applied an exponential decay function (Equation 10) that links the plant removal fraction to the effective K_d for each compound–biochar–soil combination. Where b is determined by solving for the rate constant which best fits the Kd to removal efficiency, as described in Section 1.7 This is the same Equation 5. used in Section 1.7 to model plant uptake for phytoremediation; however, instead of decreasing K_{oc} to enhance uptake, in this context, K_d is increased through the addition of biochar to reduce plant uptake. To ensure model predictions remained realistic, we incorporated a scaling parameter (min_eff) into the exponential uptake equation. This value represents the minimum observed plant removal efficiency at the highest measured K_d and reflects the fact that PFAS uptake by plants rarely reaches zero. By anchoring the exponential decay curve with min_eff, the model captures both the empirical lower bound of uptake and the diminishing bioavailability of PFAS as sorption increases (Fig S6).

$$\text{Removal}_t = \text{min\_eff} \times \exp\left(b \times \left(K_d - K_{d,\max}\right)\right) \quad (13)$$

Risk based thresholds for plant concentrations

To contextualize the significance of limiting PFOS uptake into plant biomass through biochar amendment, we compared the modeled PFOS concentrations in hemp to risk-based thresholds developed for the agronomic exposure pathway of soil to milk through grazing on impacted land.(*70*)

The most stringent, available screening level was the Maine CDC's PFOS soil screening level (SSL) for dairy farms, which is based on preventing exceedance of a milk PFOS action level of 210 ng/L (*70*). While SSLs are reported as soil concentrations, the derivation methods include published soil-to-plant transfer factors (TF_{plant}) and mass loading factors (MLF), which were used to back-calculate a plant tissue threshold corresponding to this milk protection goal. These parameters are summarized in Table S5. The equation below was applied to convert the soil-based SSL into a corresponding PFOS concentration in plant tissue (dry weight)

$$C_{plant} = C_{soil} * \left(TF_{plant} + MLF\right) \quad (14)$$

Enhanced weathering CDR estimates

CDR from ERW was estimated using the reactive transport model SCEPTER(*36*, *37*, *71*). Kanzaki et al. (2025) conducted ensembles of ERW simulation on CONUS croplands (defined as the area where >10% land use is for cropland) at 1°x1° resolution. Their experiments were repeated here but extended to all CONUS areas. In a brief summary, ERW experiment procedure was as follows:

(1) models were initialized to reproduce observed soil pH, base saturation, soil organic carbon contents, and soil pCO_2.

(2) Two ensembles of ERW experiments were conducted for 100 model years, by adding either CaO or basalt, to the initialized models so that at the end of each year, target soil pH = 7 is satisfied.

We utilized 1°x1° grid products used by Kanzaki et al. (2025) as input to the model, including temperature, soil moisture, runoff/infiltration, cation exchange capacity, nitrification rate, soil erosion, soil porosity, net primary production (NPP) (see their Table 1), excluding those used as observation targets for the model to reproduce (soil pH, base saturation, soil organic carbon contents, and soil pCO_2 which is calculated with NPP and temperature). Model setup is simplified as described in Kanzaki et al. (2024, 2025) where simulated solid phases are limited to a bulk soil phase plus a soil organic matter both of which are assumed to have the same cation exchange properties. Aqueous species tracked in the model include Ca, Mg, Na, K, Si and NO_3 and gaseous CO_2 is tracked as well. Model's boundaries are specified with fixed compositions at the top for aqueous and gaseous phases, while at the bottom for solid phase where gaseous and aqueous diffusions are not allowed. Four model parameters are tuned during the initialization process [(1) above]. They include a parameter for cation exchange between Na and H, Ca concentration at the top boundary, organic matter input to the model and turnover time for organic matter. Cation exchanges among cations (e.g., Ca-H, Mg-H) are all scaled with the Na-H exchange so tuning of the Na-H exchange parameter, along with Ca concentration at the top boundary, enabled the model to reproduce observed soil pH and base saturation. Tuned Ca concentrations can be regarded as representing cation inputs to the model from the historical ag liming plus background weathering. See Supplementary material of Kanzaki et al. (2025) for more details on the tuned parameters.

In the model, soil CO_2 was tracked which enabled direct estimation of CDR either through reduction of CO_2 emission to the atmosphere or increase of DIC through porewater advection,

which converge within a couple of porewater residence time. We take the former method (CDR as reduction of soil CO_2 emission) for our CDR calculation. This choice does not affect our CDR calculation by ERW.

Transport of ERW feedstock estimates

To model transport for EW material, stochastic ranges were established using existing literature to simulate three scenarios: semi-truck transport, semi-truck and barge transport, and semi-truck and rail transport.

To calculate the amount of rock material available for EW application M, the maximum load of a semi-truck L_T was multiplied by the inefficiency due to the grinding process i_g. From equation 13, the available ion content was calculated by multiplying M by the inefficiency resulting from losses of ions to the ocean, representing the initial weathering potential of the parent material.

$$M = L_T \times (1 - i_g) \qquad (15)$$

$$C_{available} = M \times (1 - i_o) \qquad (16)$$

Equation 15 calculates the potential CDR of EW application of rock material transported. To do this, the result of Equation 14 is multiplied by C_c, the fraction of the parent material weatherable for CDR, which has a stochastic range of 0.20 to 0.30. This is assumed to represent the tons of CO2 removed upon basalt application at the site.

$$CDR_{site} = C_{available} \times C_c \qquad (17)$$

To find the emissions associated with transport of ERW material, scenarios were simulated assuming a fully loaded semi-truck transporting material to the application site. Fuel efficiency was established in two stochastic ranges for a fully loaded truck F_f, and an empty truck on return trips F_e, with ranges of [9.66 , 12.87] and [10.46 , 12.87] respectively. The average CO2

emissions for diesel fuel E_d were established from the literature at 0.01119 t/gal. Equations 16 and 17 show the emissions for a full (E_{km}) and empty ($E_{km\ empty}$) semi truck. A 25% discount was applied to emissions for the return, under the assumption that industrial transport operates as a network, making some trips one-way.

$$E_{km} = \frac{E_d}{F_f} \qquad (18)$$

$$E_{km\ empty} = 0.75 \times \frac{E_d}{F_e} \qquad (19)$$

Total emissions for truck transport were then calculated using the emissions for each trip multiplied by the trip distance d_t. Trip distances were kept in the stochastic range of 10 to 1000 km.

$$E_{total\ truck} = (E_{km} \times d_t) + (E_{km\ empty} \times d_t) \qquad (20)$$

To establish a percentage inefficiency due to transport e_r, the total emissions from truck transport were divided by CDR in a perfectly efficient scenario ($CDR_{perfect}$).

$$e_r = \frac{E_{total\ truck}}{CDR_{perfect}} \qquad (21)$$

An index of acceptable scenarios from the Monte Carlo simulation were created, limiting the sum of the inefficiencies e_r,i_o, and i_g to equal to the target inefficiency i_t, with a ±1% tolerance range . Target inefficiencies of $i_t = 0.25$ and $i_t = 0.30$ were simulated to produce two maximum distances.

$$-0.01 \leq (e_r + i_o + i_g) - i_t \leq 0.01 \qquad (22)$$

For barge transport, emissions were calculated utilizing a fuel efficiency metric F_B of 1086.3 km/gal/ton. To calculate efficiency per distance $F_{B\ cargo}$, the unit fuel efficiency was multiplied

by the sum of the load L_T and the weight of the barge container w_B in Equation 8. The same load L_T is utilized in calculating semi-truck transport, as it is the limiting factor in cargo capacity for one trip to and from barge transport.

$$F_{B\ cargo} = F_B \times (L_T + w_B) \quad (23)$$

To calculate the total emissions of barge transport $E_{total\ barge}$, the rate of emissions per kilometer was first calculated in Equation 22 by dividing the emissions from one gallon of diesel fuel E_d by the fuel efficiency of material transport $F_{B\ cargo}$. Multiplying this quotient by the distance transported by barge d_b in Equation 23 results in the total emissions of barge transport $E_{total\ barge}$. d_b was assigned the stochastic range of 200-3000 km.

$$E_{km\ barge} = \frac{E_d}{F_{B\ cargo}} \quad (24)$$

$$E_{total\ barge} = \left(E_{km\ barge} \times d_b\right) \quad (25)$$

Semi-truck emissions were calculated using the same method as detailed in the previous section, with an alteration of its stochastic range d_T to [10 , 50]. The emissions ratio $e_{r\ barge}$ was calculated by dividing the sum of the truck emissions to barge transport and total emissions resulting from barge transport by perfectly efficient CDR.

$$e_{r\ barge} = \frac{\left(E_{total\ truck} + E_{total\ barge}\right)}{CDR_{perfect}} \quad (26)$$

An index of acceptable scenarios from the Monte Carlo simulation were created, limiting the sum of the inefficiencies $e_{r\ barge}$,i_o, and i_g to equal to the target inefficiency i_t, with a ±1% tolerance range (Equation 20). Target inefficiencies of $i_t = 0.25$ and $i_t = 0.30$ were simulated to produce two maximum distances.

For rail transport, emissions rates E_R were calculated from an established emissions range of 0.0002-0.00004 tCO2/t/km based on literature review. To calculate emissions per distance $E_{km\,rail}$, E_R was multiplied by the sum of the load L_T and the weight of the barge container w_R. The same load L_T is utilized in calculating semi-truck transport, as it is also the limiting factor in cargo capacity for one trip to and from rail transport.

$$E_{km\,rail} = E_R \times (L_T + w_R) \quad (27)$$

To calculate the total emissions of rail transport $E_{total\,rail}$, $E_{km\,rail}$ was multiplied by the distance transported by rail d_r in Equation 13. d_r was assigned the stochastic range of 100 to 1000 km.

$$E_{total\,rail} = (E_{km\,rail} \times d_r) \quad (28)$$

Semi-truck emissions were calculated using the same method as detailed in the previous section, with an alteration of its stochastic range d_T to [10 , 50]. The emissions ratio $e_{r\,rail}$ was calculated by dividing the sum of the truck emissions to rail transport and total emissions resulting from rail transport by perfectly efficient CDR.

$$e_{r\,rail} = \frac{(E_{total\,truck} + E_{total\,rail})}{CDR_{perfect}} \quad (29)$$

An index of acceptable scenarios from the Monte Carlo simulation were created, limiting the sum of the inefficiencies $e_{r\,rail}$,i_o, and i_g to equal to the target inefficiency i_t, with a ±1% tolerance range. Target inefficiencies of $i_t = 0.25$ and $i_t = 0.30$ were simulated to produce two maximum distances.

Biochar CDR Estimation

We estimated the potential net CDR from biochar production applied across impacted agricultural land throughout the contiguous United States. This analysis incorporated spatial variability in biomass productivity and amount of PFAS impacted land to produce biomass yields. Impacted land area and its spatial location was determined as previously described above in section S1.2. In short the median amount of impacted land determined at 1.22 million hectares was broken into 1,000 hectare grid cells and distributed into states based on biosolid application data, then distributed within each state based on population densities. For each 1,000-hectare grid cell, we calculated the net CDR using Monte Carlo simulation of biomass conversion and emissions factors.

To reflect variation in growing season and biomass productivity, biomass yield (Y_b) was scaled linearly with latitude for each coordinate in the dataset. Latitude was normalized across the national domain, and yields were interpolated between a minimum and maximum value:

$$Y_{\mathrm{b}} = Y_{\max} - \left(\frac{\mathrm{lat}_{\max} - \mathrm{lat}_{\min}}{\mathrm{lat} - \mathrm{lat}_{\min}} \right) \cdot (Y_{\max} - Y_{\min}) \quad (30)$$

The yield for that specific grid cell was then used to determine the mass of biochar produced using the area of the total grid cell (1,000 ha) and the Biochar conversion efficiency (η) of the pyrolizer:

$$B_{\mathrm{char}} = Y_b \cdot A \cdot \eta \quad (31)$$

The CDR of the biochar at each cell was then determined by converting biochar to its equivalent mass of carbon and the stoichiometric ratio of C to CO_2 equal to 3.67:

$$\mathrm{CDR}_b = \mathrm{B}_{char} \cdot \mathrm{C}_f \cdot 3.67 \quad (32)$$

Losses were also accounted for from pyrolysis and transport of biomass and biochar. The median transport losses were ~1.5 % and pyrolysis losses were ~7%. Transport emissions were estimated by calculating the number of truck trips required to move biomass, multiplied by round-trip distance and fuel efficiency. Emissions were then derived from the diesel emission factor, where C_{truck} is truck capacity (t/load), d is the round-trip transport distance (km), F_f is the vehicle fuel efficiency (L km^{-1}), and ϵ_{diesel} is the diesel emission factor (kg CO_2 L^{-1}).

$$\mathrm{Trips} = \frac{B}{C_{\mathrm{truck}}} \quad (33)$$

$$E_{\mathrm{transport}} = \mathrm{Trips} \cdot d \cdot F_{\mathrm{f}} \cdot \epsilon_{\mathrm{diesel}} \quad (34)$$

Pyrolysis emissions were expressed as the emissions per ton of biomass processed were ϵ_{pyro} is the pyrolysis emission rate (kg CO_2 t^{-1}).

$$E_{\mathrm{pyrolysis}} = \epsilon_{\mathrm{pyro}} \cdot B \quad (35)$$

These two sources of loss were then subtracted from the total CDR calculated from the biochar production to result in a net CDR.

$$\mathrm{CDR}_{net} = \mathrm{CDR}_{biochar} - \mathrm{e}_{trucking} - \mathrm{e}_{pyrolysis} \quad (36)$$

We acknowledge that long term/ permanent storage would require an in-depth assessment of decay rates across the U.S. and with production temperatures so a 10% loss was then assumed for all CDR following application (*72*). The resulting CDR was then assumed to be long term storage. All parameters for these calculations are presented in Table S6 below.

Traditional remediation emission estimates and costs

To model transport for PFAS contaminated soils to traditional remediation sites, stochastic ranges were established using existing literature to simulate two scenarios: semi-truck transport and semi-truck and rail transport. Models simulated transport to a hazardous waste landfill, as well as a rotary kiln, to show alternative scenarios and the associated emissions of carbon dioxide.

Semi-truck transport was calculated using the same method as calculations done for the transport of biomass material in an earlier section. The same load size, fuel efficiencies, and emissions due to the combustion of diesel fuel were used. Semi-trucks were assumed to be fully loaded, with a large discount on backhauls assuming a short reposition distance d_d for the next job. To calculate the number of farms impacted by PFAS contamination across the United States, the 1.2 million ha of impacted land i calculated previously was divided by the average farm size a_f:

$$f_i = \frac{i}{a_f} \qquad (37)$$

The weight of soil per ha was then calculated, multiplying average soil density by the depth of soil and the conversion factor. To then find the amount of contaminated soil per farm we multiplied the average farm size by the unit weight of contaminated soil:

$$w_s = s_d \times \rho_s \times 1000 \frac{m^2}{ha} \qquad (38)$$

$$s_f = w_s \times a_f \quad (39)$$

After finding the total amount of soil removal on the individual farm scale, the number of trips required for transport of the soil to an external site was calculated by dividing the amount of soil per farm by the maximum load size of a semi-truck and rounded up to the nearest whole number.

$$t_f = \frac{s_f}{L_T} \quad (40)$$

To simulate the transport of contaminated soil to a hazardous waste landfill, distances d_l between were simulated stochastically. The emissions for each trip were calculated with average emissions for a full semi-truck being multiplied by the trip distance, as in. This product was then multiplied by the trips required per farm to get an estimate of total emissions per farm due to transport to hazardous landfill. If the distance exceeded the maximum of 120 km it was assumed a more efficient rail pathway could have been selected and rail emissions were estimated. For a unit estimate of emissions, the total truck emissions per farm was divided by the average farm size to produce emissions per hectare:

$$E_{trip\ truck\ l} = E_{km\ truck} \times d_l \quad (41)$$

$$E_{truck\ l} = E_{trip} \times t_f \quad (42)$$

$$E_{ha,truck,l} = \frac{E_{total\ truck\ l}}{a_f} \quad (43)$$

$$E_{rail\ l} = E_R \times t_r \quad (44)$$

The second scenario for contaminated soil removal involves transport of the material to a rotary kiln for thermal degradation of PFAS. Emissions associated with this process included both transport of the material to the facility as well as the emissions due to operation of the kiln. Calculations of emissions due to operation of the kiln were calculated using energy consumption

and associated emissions ranges. To calculate the number of operational hours required to process a farm's contaminated soil, the total soil per farm was divided by the kiln's hourly capacity:

$$t_k = \frac{s_f}{c_k} \qquad (44)$$

The energy consumption and associated emissions of running the kiln were then calculated by using a BTU usage (MMBtu/hr) for processing contaminated soils, assumed based on literature reports see Table S7. To calculate BTUs required per farm, the amount of time to process a farm's contaminated soils was multiplied by a kiln's hourly BTU consumption. The associated emissions were calculated using a range of emissions from differing fuel sources multiplied by the BTU usage per farm.

$$BTU_{farm} = u_{BTU} \times t_k \qquad (45)$$

$$E_k = E_{BTU} \times BTU_{farm} \qquad (46)$$

Transport was calculated in the same manner as for the landfill scenario, but with a different trip distance range. Additionally, the kiln was assumed to oxidize all soil organic matter to CO_2, adding to the total emission burden. This was calculated by multiplying the total soil mass by the fraction of organic matter f_{OM}, the fraction of carbon within the organic matter $f_{C|OM}$, and the stoichiometric conversion factor from carbon to CO_2 (≈3.67 by mass).

$$E_{OM} = s_f * f_{OM} * f_{C|OM} * 3.6 \qquad (47)$$

The total emissions associated with truck transport for soil remediation via rotary kiln was first calculated at a farm level, taking the sum of the emissions due to kiln operation and material

transport to the facility. A unit estimate was then taken by dividing the calculated value by the average farm size. The results of these emission estimates are shown in Fig S7.

$$E_{total\ truck\ k} = E_k + E_{truck\ k} \qquad (48)$$

$$E_{ha,truck,k} = \frac{E_{total\ truck\ k}}{a_f} \qquad (49)$$

Cost estimates were based on prior work that established unit cost benchmarks for the remediation and disposal of PFAS-contaminated soils under U.S. Superfund site management(*16*). The previously estimated total soil mass across 1.2 million ha of impacted land was multiplied by the per-ton cost estimates from that report, resulting in approximately $1.3 trillion for hazardous-waste landfill disposal and $2.4 trillion for thermal treatment (Fig S8).

Cost of Biochar Production

Biochar production cost analyses were simulated under two conditions. Large pyrolysis facilities operated under the assumption of requiring material transport—transporting biomass and returning biochar—by semi-truck. Mobile pyrolysis rigs operated without transport requirements, but included labor, fuel and start-up costs. To capture technical and economic differences between scenarios, the unit cost per ton of CDR was calculated and depicted on a histogram in Fig S8. All values or ranges for parameters are in Table S8.

For large pyrolysis facilities, the biomass consumption rate B_L and hourly operational cost O_L were defined as stochastic input parameters. Hourly biochar production $c_{h,L}$ was determined by multiplying the biomass input rate by the biomass-to-biochar conversion factor b_{bc}. The resulting hourly production was scaled by the total operating hours of the facility T_L to obtain daily biochar output $c_{d,L}$. The corresponding daily biomass throughput $B_{d,L}$ was similarly computed as the product of the biomass input rate and operating time.

$$c_{h,L} = B_L \times b_{bc} \quad (50)$$

$$c_{d,L} = c_{h,L} \times T_L \quad (51)$$

$$B_{d,L} = B_L \times T_L \quad (52)$$

The carbon content of the produced biochar $C_{d,L}$ was calculated by multiplying the daily biochar production $c_{d,L}$ by the biochar carbon fraction C_{BC}. The total potential carbon dioxide removal $CDR_{d,L}$ was then determined by converting the stored carbon to its equivalent mass of CO_2 using the stoichiometric conversion constant c_{cc}.

$$C_{d,L} = c_{d,L} \times C_{BC} \quad (53)$$

$$CDR_{d,L} = C_{d,L} \times c_{cc} \quad (54)$$

Economic analyses of biomass (both forestry and agricultural residue) markets provided stochastic estimates of the unit biomass price P_B, which was used to calculate the total daily feedstock cost for the facility. The daily biomass cost $P_{B,d,L}$ was determined by multiplying the unit biomass price by the total biomass processed $B_{d,L}$, assuming continuous operation at full capacity.

$$P_{B,d,L} = P_B \times B_{d,L} \quad (55)$$

Because large stationary pyrolysis systems require external transport, material delivery and product return were incorporated into the model. The number of daily biomass deliveries $t_{d,L}$ was calculated by dividing the total daily biomass processed $B_{d,L}$ by the truck load capacity L_T. Return trips for biochar transport were determined using the same approach, substituting daily biochar production $c_{d,L}$ for biomass throughput.

$$t_{d,L} = \frac{B_{d,L}}{L_T} \qquad (56)$$

$$t_{return\ d,L} = \frac{c_{d,L}}{L_T} \qquad (57)$$

Emissions associated with transport were estimated following the same methodology used in the transport economics framework. The emission rate per kilometer $E_{km}$was calculated by dividing the diesel emission factor $E_d$by the average fuel efficiency of a fully loaded truck F_f. Emissions for each trip E_{trip}were then obtained by multiplying the per-kilometer emission rate by the transport distance d_t. The total transport emissions $E_{total}$for the large pyrolysis facility were determined by summing the emissions from both biomass delivery trips $t_{d,L}$and biochar return trips $t_{return,d,L}$.

$$E_{trip} = E_{km} \times d_t \qquad (58)$$

$$E_{total} = (E_{trip} \times t_{d,L}) + (E_{trip} \times t_{return\ d,L}) \qquad (59)$$

Transportation costs were estimated using a per-distance operating cost for semi-truck transport P_{km}, derived from literature sources. The total cost per trip $P_{drive}$was calculated by multiplying $P_{km}$by the transport distance d_t. Daily transport cost $P_{transport}$was then determined by multiplying $P_{drive}$by the number of biomass delivery trips $t_{d,L}$and biochar return trips $t_{return,d,L}$, and summing the two components to represent the total transport expense for a fully operational facility.

$$P_{transport} = \left(P_{drive} \times t_{d,L}\right) + \left(P_{drive} \times t_{return\ d,L}\right) \qquad (60)$$

Total system cost calculations incorporated both operational and material expenses. Given that large pyrolysis facilities often generate their own power and heat through biogas and biofuel, with these co-products being quite valuable on the open market. Thus, depending on the extent of

a given operator's utilization of these co-products, operation of large sites can range from being entirely covered by the co-products, such that the biochar is a by-product, to being exclusively used for the continuation of the reaction. The daily operational cost $O_{d,L}$ was determined by multiplying the facility's operating time T_L by its stochastic hourly operational cost O_L. The overall daily cost $P_{total,L}$ was then computed as the sum of transport costs $P_{transport}$, operational costs $O_{d,L}$, and biomass feedstock costs $P_{B,d,L}$, representing the total expenditure required for continuous operation of the large pyrolysis facility

$$P_{total,L} = P_{transport} + O_{d,L} + P_{B,d,L} \quad (61)$$

The unit cost of carbon dioxide removal $P_{CDR,L}$ for large pyrolysis facilities was calculated by dividing the total daily system cost $P_{total,L}$ by the net amount of carbon dioxide removed $CDR_{net,L}$. This metric represents the cost per ton of CO_2 effectively sequestered after accounting for all emissions and operational expenses associated with the process.

$$P_{CDR,L} = \frac{P_{total,L}}{CDR_{net,L}} \quad (62)$$

For mobile pyrolysis units, the biomass consumption rate B_M and hourly operational cost O_M were defined as stochastic input parameters to reflect variability in small-scale system performance. Calculations followed the same methodology as those for the large stationary facility. Hourly biochar production $c_{h,M}$, daily biochar production $c_{d,M}$, and total daily biomass processed were computed using the corresponding relationships among biomass input rate, conversion efficiency, and operating hours T_M. The range of operational hours for mobile units was defined to capture typical variability observed across field-scale deployments.

$$c_{h,M} = B_M \times b_{bc} \quad (63)$$

$$c_{d,M} = c_{h,M} \times T_M \quad (64)$$

$$B_{d,M} = B_M \times T_M \quad (65)$$

The carbon content of the biochar, overall carbon dioxide removal potential, and daily biomass cost for mobile units were calculated using the same relationships established for the large facility. Specifically, the carbon content was determined from the daily biochar production and carbon fraction, the CDR potential was obtained by converting stored carbon to its CO_2 equivalent, and the daily biomass cost was calculated as the product of unit biomass price P_B and total biomass processed $B_{d,M}$.

$$C_{d,M} = c_{d,M} \times C_{BC} \quad (66)$$

$$CDR_{d,M} = C_{d,M} \times c_{cc} \quad (67)$$

$$P_{B,d,M} = P_B \times B_{d,M} \quad (68)$$

Mobile pyrolysis units offer the advantage of on-site operation, eliminating the need for transport of biomass or biochar and thereby reducing associated emissions and costs. Consequently, their economic calculations differ from those of large stationary systems. Fuel use was incorporated as a primary operational expense, with average hourly fuel consumption F_M used to estimate total daily fuel use $F_{d,M}$ by multiplying F_M by the total operational hours T_M. The corresponding daily fuel cost $P_{F,d,M}$ was then calculated by multiplying the total fuel consumed by the unit price of diesel fuel P_{fuel}.

$$F_{d,M} = F_M \times T_M \quad (69)$$

$$P_{F,d,M} = F_{d,M} \times P_{fuel} \quad (70)$$

Purchasing a mobile pyrolysis unit represents a significant upfront capital investment P_M, which includes equipment cost, installation, and operator training. To incorporate this expense into the daily cost framework, the total capital cost was normalized over a representative 330-day operating season, providing a daily equivalent investment cost. Daily operational costs $O_{d,M}$were then calculated by multiplying the hourly operating cost $O_M$by the total number of operating hours per day T_M.

$$P_{M\ inital} = \frac{P_M}{90\ days} \qquad (71)$$

$$O_{d,M} = T_M \times O_M \qquad (72)$$

Total daily system costs for the mobile pyrolysis unit $P_{total,M}$were calculated as the sum of normalized capital investment $P_{Minitial}$, operational costs $O_{d,M}$, biomass feedstock costs $P_{B,d,M}$, and daily fuel costs $P_{F,d,M}$. Emissions from the mobile system $E_{d,M}$were estimated using fuel efficiency data, with the diesel emission factor $E_d$divided by the fuel efficiency $F_M$and multiplied by the total operational hours $T_M$to determine daily CO_2 emissions associated with system operation.

$$P_{total,M} = P_{Minitial} + O_{d,M} + P_{B,d,M} + P_{F,d,M} \qquad (73)$$

$$E_{d,M} = \frac{E_d}{F_M} \times T_M \qquad (74)$$

Net carbon dioxide removal $CDR_{net,M}$and the corresponding cost per ton of removal $P_{CDR,M}$for mobile pyrolysis units were calculated using the same methodology applied to the large facility. Net CDR was determined by subtracting operational emissions $E_{d,M}$from the gross CDR potential, and the unit cost of removal was obtained by dividing the total daily system cost $P_{total,M}$by the net amount of CO_2 removed.

$$CDR_{net,M} = CDR_{d,M} - E_{d,M} \quad (75)$$

$$P_{CDR,M} = \frac{P_{total,M}}{CDR_{net,M}} \quad (76)$$

Results of the cost per ton of CDR for each method are displayed in a histogram in Fig S9.

Remediation cost estimates

For the net annual cost of remediation (NC), a stochastic framework was developed to account for both costs and revenues associated with the proposed approach. The model incorporated: (i) annual operational costs for cultivating hemp and fescue/hay, (ii) annual payments to farmers for participation and labor, (iii) deployment costs for biochar and enhanced rock weathering (ERW), and (iv) revenues from the sale of CDR credits generated from biochar and ERW. Deployment costs and CDR credit revenues for each technology were scaled according to the CDR rate, reflecting their correlation (e.g., reduced biomass production lowers transport and operational costs but also decreases biochar output and total CDR achieved). This net annual cost was then calculated per iteration (N = 100,000) and per year (t). in the equation below:

$$\begin{aligned} NC_{i,t} = {} & C_{\text{hay},t} + C_{\text{hemp},t} + I_{\text{farmer},t} + P_{\text{biochar},i} \cdot Q_{\text{biochar},t} \\ & + P_{\text{ERW},i} \cdot Q_{\text{ERW},t} - S_{\text{biochar},t} \cdot Q_{\text{biochar},t} - S_{\text{ERW},t} \cdot Q_{\text{ERW},t} \end{aligned} \quad (77)$$

The total remediation cost was calculated by summing the net annual remediation costs over the duration of each scenario (T), where T was drawn from a truncated normal distribution ($\mu = 22.5$, $\sigma = 4.5$) bounded between 10 and 60 years to reflect realistic deployment limits (parameters shown in Table S9).

$$TC_i = \sum_{t=1}^{T_i} NC_{i,t} \quad (78)$$

Breakeven cost scenarios

As the price of CDR credits from biochar and ERW sales directly influences the net annual cost of remediation, this parameter was explored to show have prices of CDR influence the remediation costs. In the model, assumed CDR prices were based on current market sales; however, these values do not account for potential overpayments an organization might accept in exchange for the co-benefits of PFAS remediation and supporting small farmers. To explore this effect, the total average sale price of CDR credits was varied and plotted against the total remediation cost to assess how market price fluctuations influence the financial burden of remediation. The first step in this process was to calculate the average CDR price using the equation below:

$$P_{\text{combined},i} = \frac{S_{\text{biochar},i} \cdot Q_{\text{biochar},i} + S_{\text{ERW},i} \cdot Q_{\text{ERW},i}}{Q_{\text{biochar},i} + Q_{\text{ERW},i}} \quad (79)$$

Once a combined CDR price was calculated, it was incorporated into the above equation to estimate the annual net costs across a range of scenarios, from no carbon credit revenue (i.e., zero CDR sales) to an upper bound of 275 USD t^{-1}, at which point average remediation costs approached zero. This analysis was performed stochastically, with 1,000 price points uniformly sampled between 0 and 275 USD t^{-1}. For each price point, 400 simulations were conducted, and the mean net cost was recorded. The standard deviation across simulations was used to derive the 10th and 90th percentile ranges for each price level. The results of the are shown in Fig S10.

2.0 FIGURES

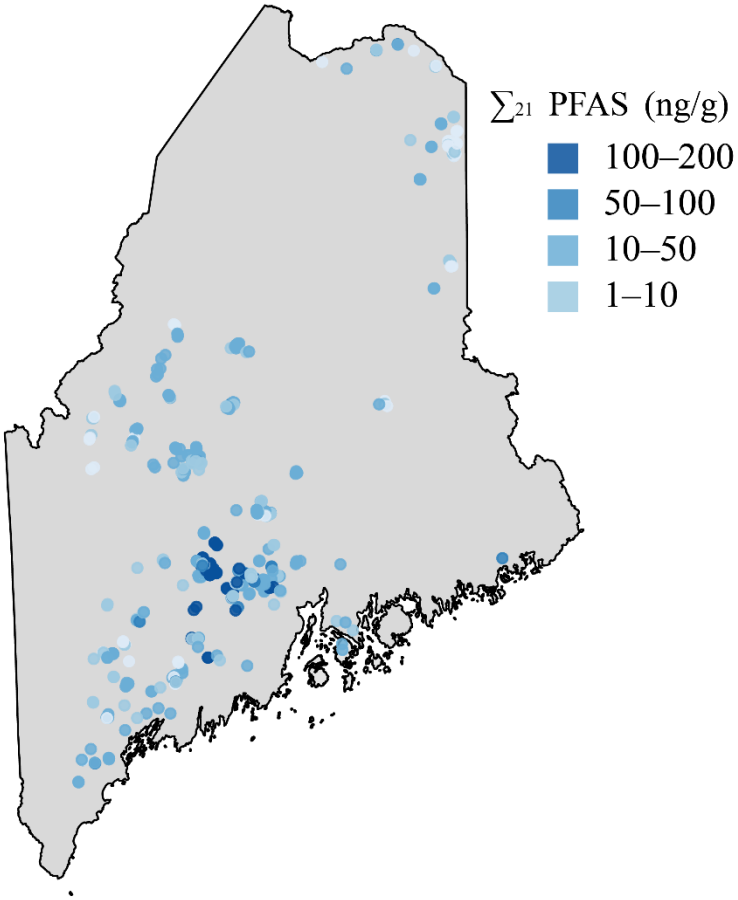

Fig S1: Distribution of impacted farmland across the state of Maine and total $\sum_{21}$ PFAS concentrations at the different sites tested (n= 563)

5

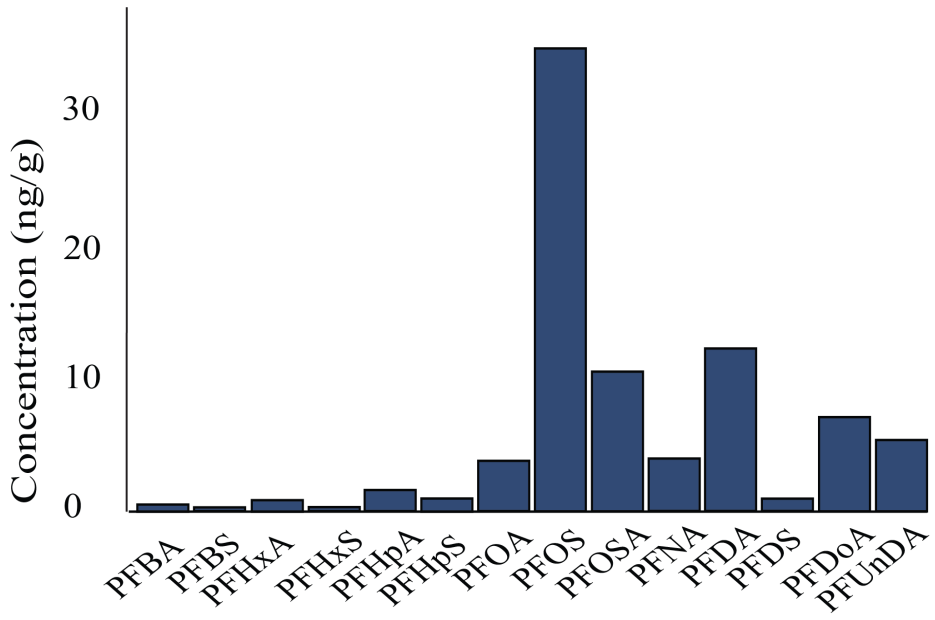

Fig S2. Concentration of 21 PFAS across the Maine DEP dataset (n=563)

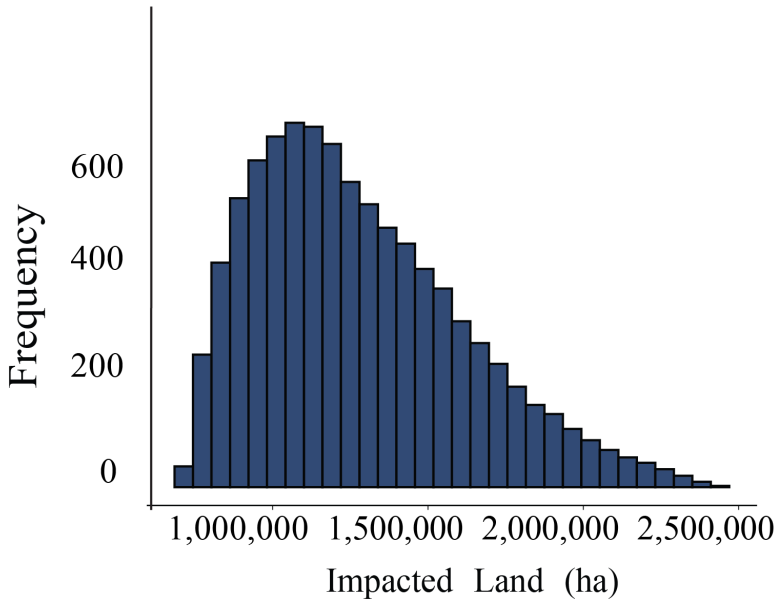

Fig S3. Probability distribution of the estimated total area of PFAS-impacted land in the United States.

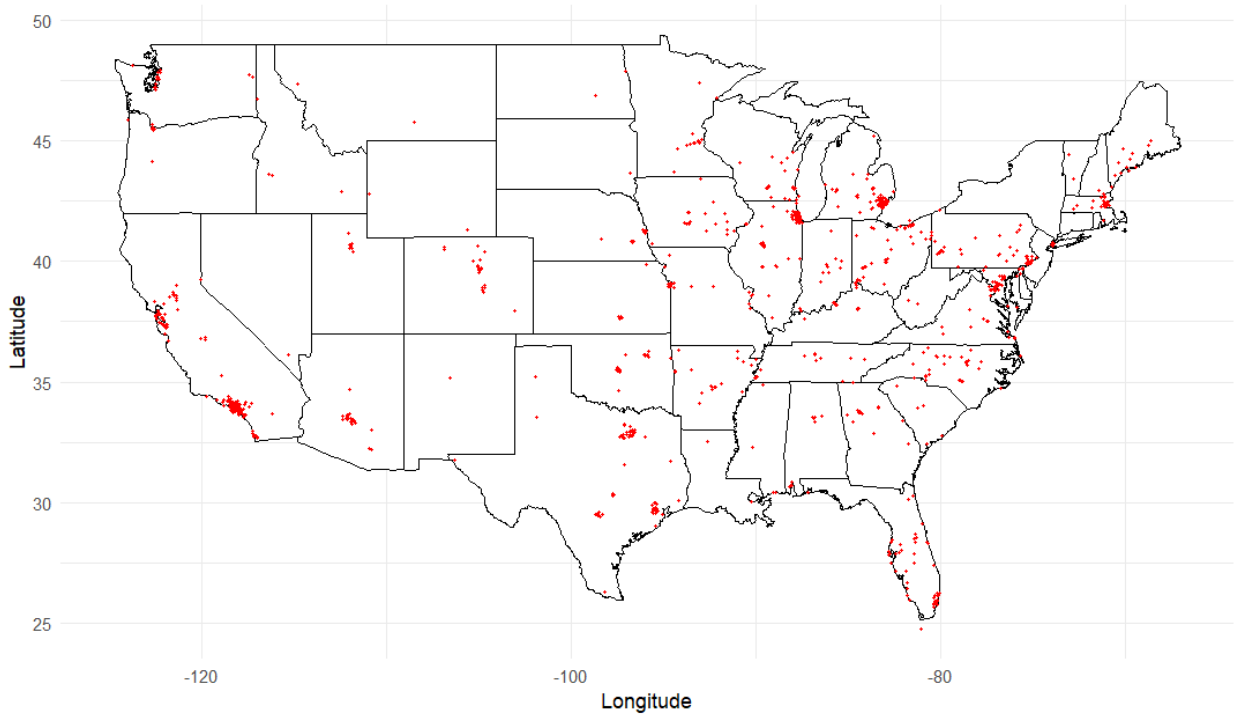

Fig S4. Spatial distribution of 1,000 hectare plots of PFAS impacted Agricultural land across the U.S.

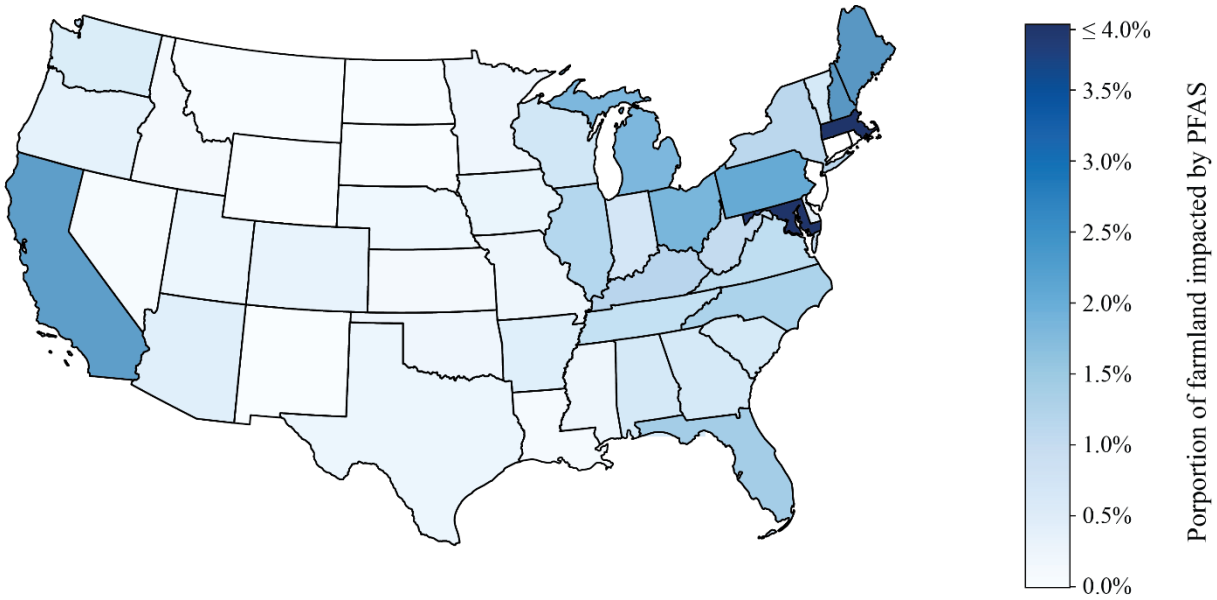

Fig S5. Proportion of the total farmland within each state that is impacted by PFAS.

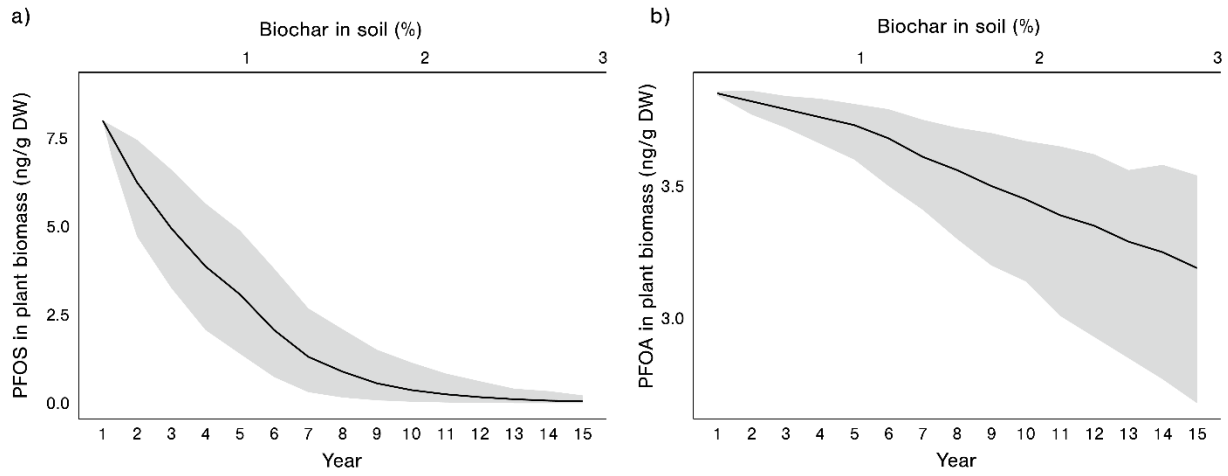

Fig S6. Concentrations of (a) PFOS and (b) PFOA in plant tissue over time as increasing amounts of biochar are amended to soils. The grey shaded region indicates the 90% uncertainty interval.

5

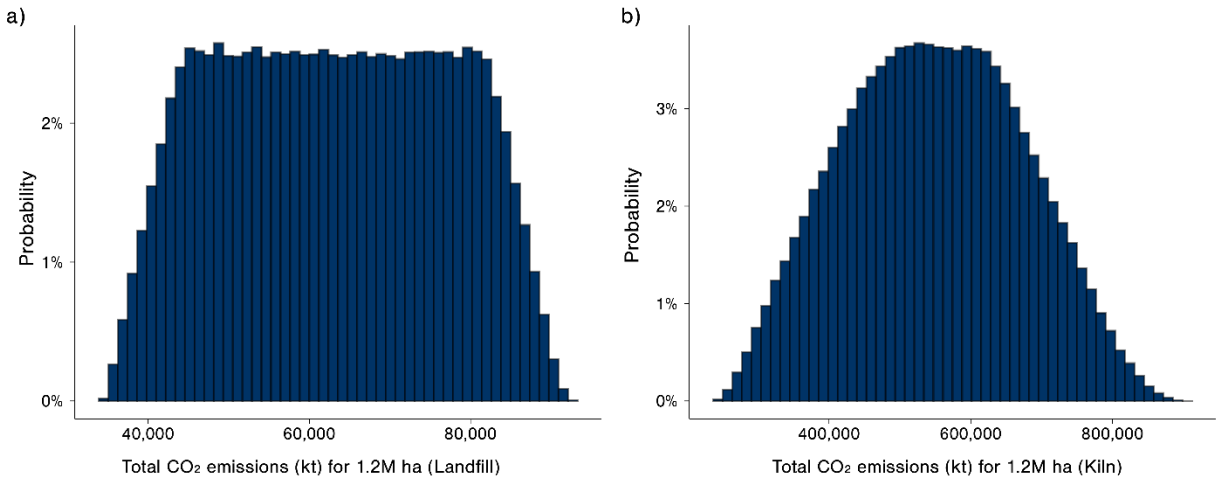

Fig S7. Probability distributions for total CO_2 emissions associated with remediating 1.2 million hectares of PFAS-impacted land.a) Landfill disposal scenario and b*)* Kiln incineration scenario. Bars represent Monte Carlo outcomes plotted as probability distributions

5

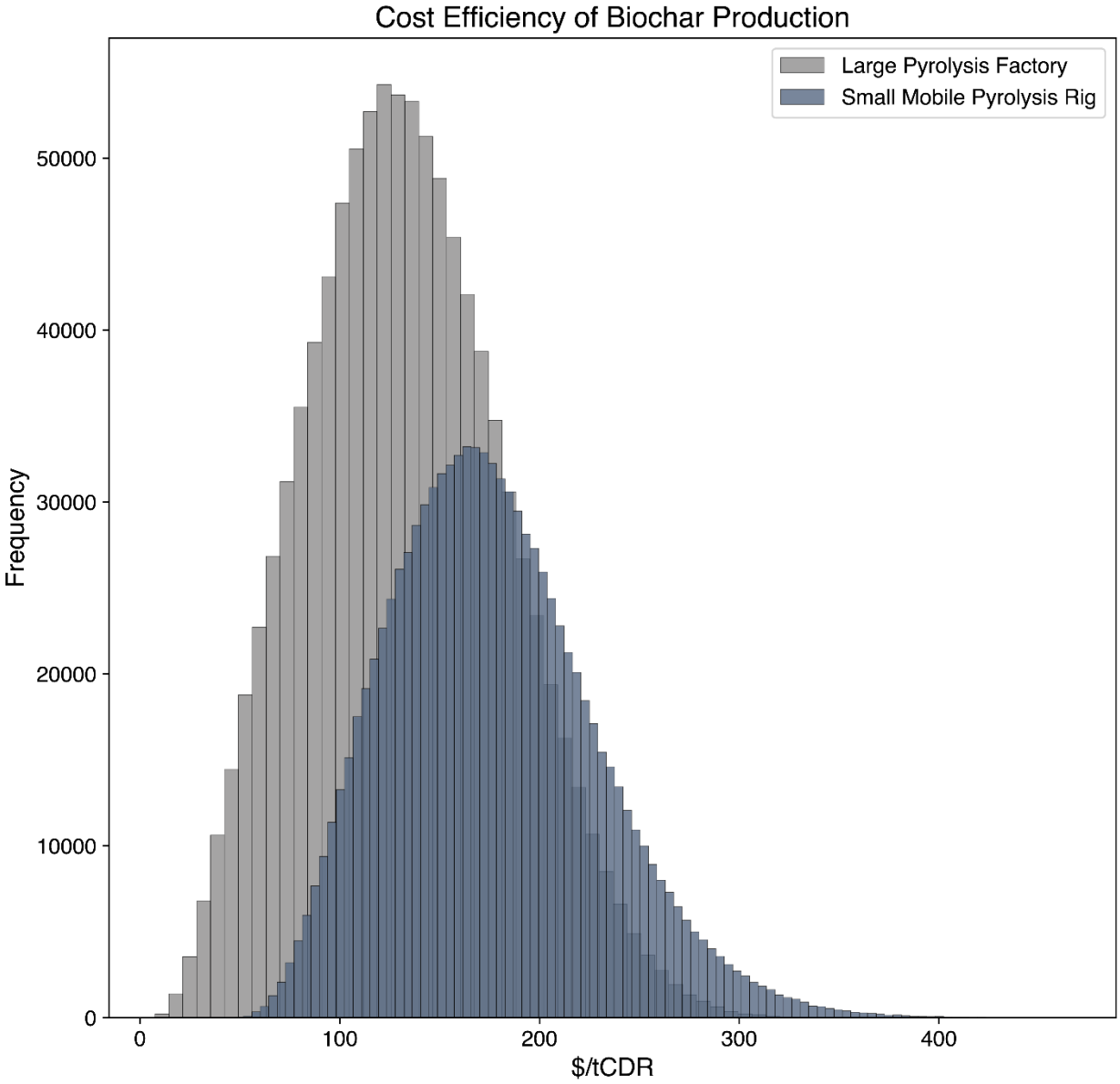

Fig S8. Results of the cost per ton of CDR between large scale pyrolysis or small transportable units

5

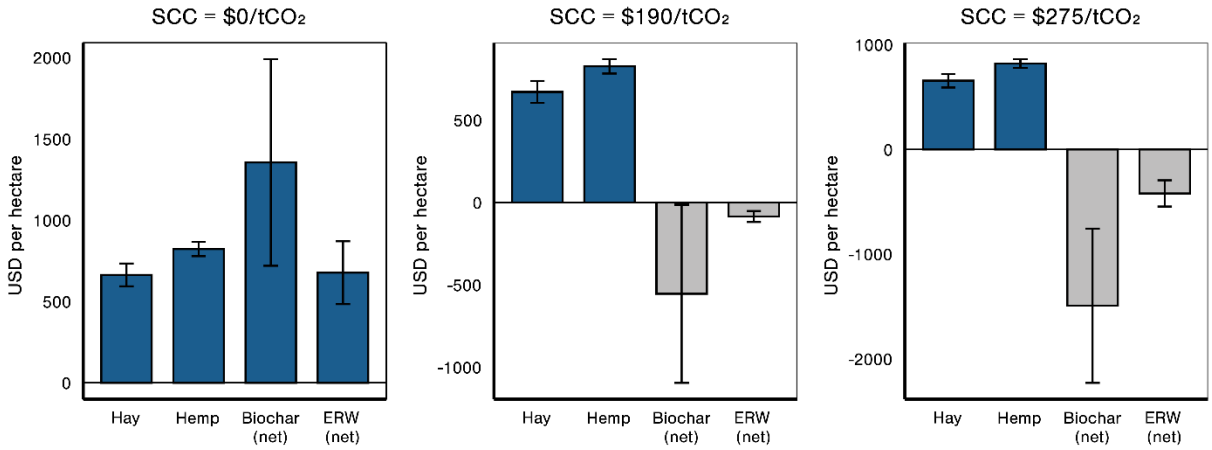

Fig S9. Cost breakdown of the major components of deployment of the remediation strategy as the social cost of carbon changes. Error bars represent one standard deviation in estimates.

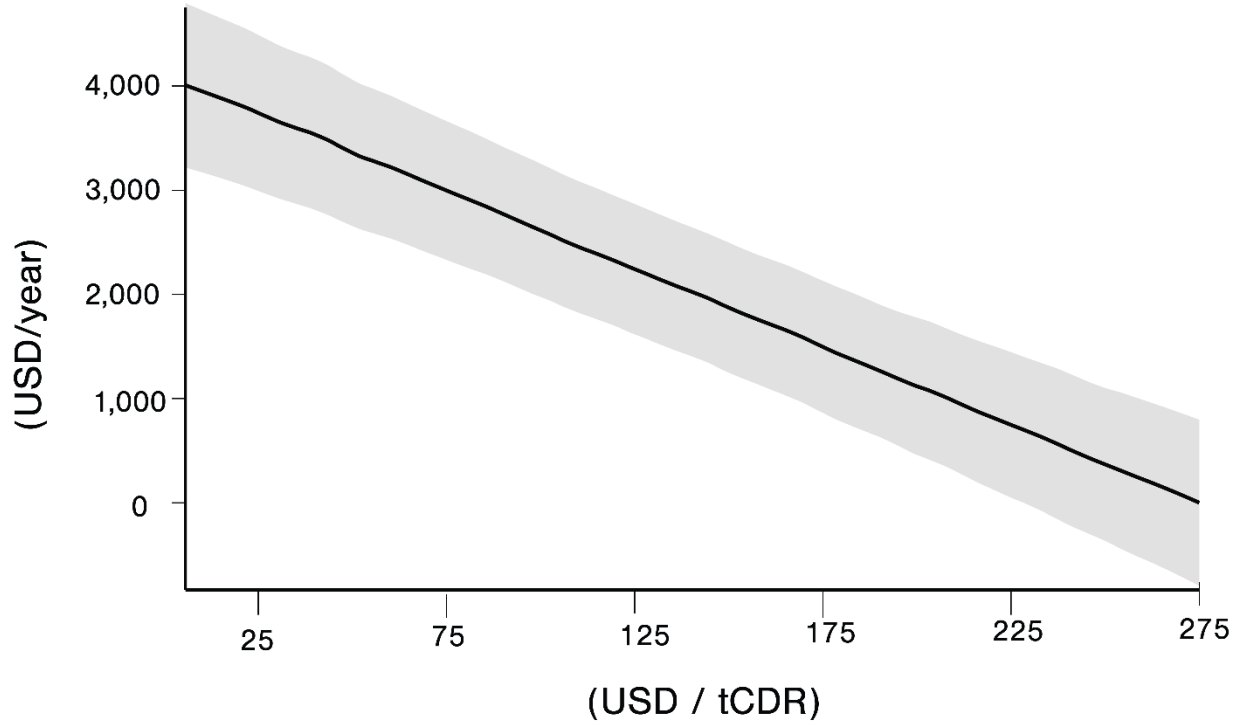

Fig S10. Break-even analysis showing the annual remediation cost per hectare as a function of the carbon dioxide removal (CDR) sale price. The gray shaded region denotes the 90% confidence interval.

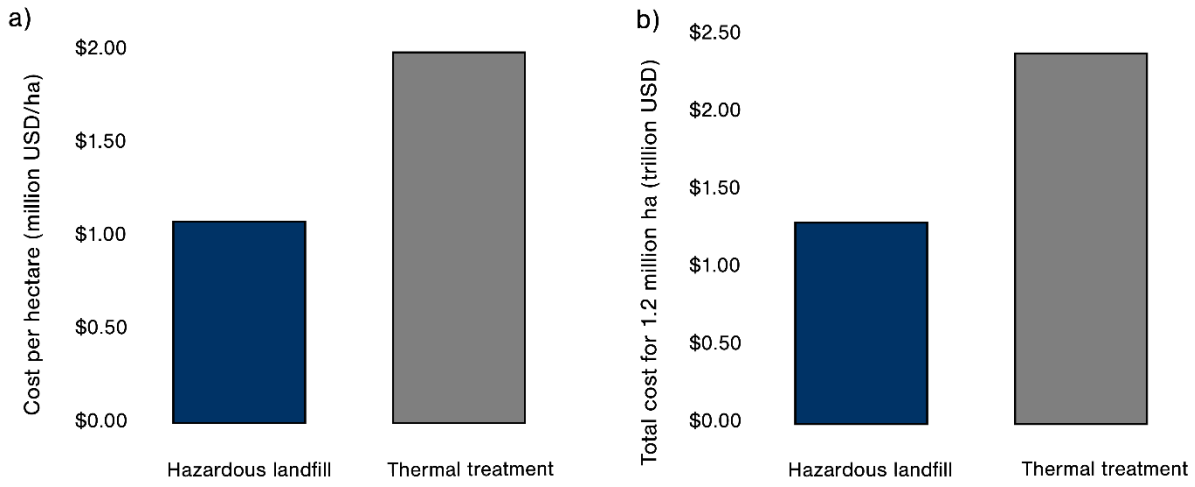

Fig S11**.** Estimated cost of conventional remediation for PFAS-impacted soils across agricultural lands. A) shows the estimated cost per hectare for excavation and disposal of contaminated soil via hazardous-waste landfill or thermal treatment. b) shows the corresponding total national cost assuming 1.2 million hectares of impacted land

3.0 TABLES

Table S1. Parameters, values, and sources for the calculation of the amount of PFAS impacted land in the U.S. from the historic application of biosolids used in equations 1-2

Parameter	Symbol	Description	Range/Value	Units	Source/Notes
Application rate	application rate	Annual biosolids application rate per hectare	6.93 – 11.03	metric tons/hectare/year	(*55*, *73*)
Duration of application	duration	Number of years biosolids were applied	7 – 15	years	(*55*, *73*)
Total application per hectare	B_h	Total applied biosolids per hectare over full application period	Derived	metric tons/hectare	Calculated
Number of simulations	n	Total Monte Carlo iterations	100,000	—	—
Cumulative biosolids applied	C_b	Total dry biosolids applied from 1970 - 2018	118,950,000	metric tons	Calculated
U.S. agricultural land area	—	Reference value for percent of total U.S. ag land impacted	175,619,491	hectares	(*57*)

Table S2. Site Condition Parameters and pH-Dependent K_{oc} Values Used in PFAS Remediation

Parameter	Symbol	Description	Range/Value	Units	Source/Notes
Initial organic carbon partition coefficient	K_{oc}, Year 0	Baseline soil organic carbon partition coefficient for PFAS	PFOS (900-1900) PFOA (250-450)	L/kg	(*18*, *61–63*)
Soil pH	pH	Soil acidity	4.5 – 6.5	Unitless	(*74*)
Fraction of organic carbon	f_{oc}	Fraction of organic carbon in soil	0.01 – 0.03	Unitless	(*75*)
Distribution coefficient	K_d	Partition coefficient between soil and water	Compound and pH-dependent	L/kg	Calculated
Maximum sorption	K_{dmax}	Maximum Kd used to scale decay based on upper limits	28 PFOA 231 PFOS	L/kg	(*63*)
Minimum uptake efficiency	min_{eff}	Minimum plant uptake fraction at highest Kd	0.01 PFOA 0.005 PFOS	unitless	Estimated Lower bound for plant uptake
Reference growing season length	G_{ref}	Duration of the baseline growing season	90	days	(*44*)
Sampled growing season length	G_s	Simulated annual growing season length	90 – 220	days	(*76*)
PFAS soil concentration	C_{soil}, Year 0	Initial soil concentration of PFAS	Median values across sites	ng/g or mg/kg	(*56*)
Hemp PFOS removal	$R_{Hemp\ 0}$	Initial removal rate of PFOS	0.53	Percent removal	(*44*)
Hemp PFOA removal	$R_{Hemp\ 0}$	Initial removal rate of PFOA	1.3	Percent removal	(*44*)
Fescue PFOS removal	$R_{Fescue\ 0}$	Initial removal rate of PFOS	3.8	Percent removal	(*65*)

Fescue PFOA removal	$R_{Fescue\ 0}$	Initial removal rate of PFOA	4.9	Percent removal	(*65*)

Table S3. Parameters of variables used to calculate biochar competitive sorption effects in equations 7-11

Parameter	Symbol	Description	Range/Value	Units	Source/Notes
Number of simulations	n	Total Monte Carlo iterations	1,000	—	—
Simulation duration	years	Total number of years modeled	20	years	—
Mean annual biochar mass	$Mass_{biochar}$	Average biochar applied each year	7.5	metric tons / ha	Calculated
SD of annual biochar mass	$Mass_{biochar,sd}$	Standard deviation of annual biochar mass	1.0	metric tons / ha	Calculated
Soil mass per hectare	Mass soil	Mass of soil in one hectare of land	3,900	metric tons	(*66*)
Organic carbon fraction	f_{oc}	Soil organic carbon content	0.02	unitless	(*66*)
Biochar-water partitioning coefficient PFOS	$K_{f\ PFOS}$	Sorption coefficient of PFOS on biochar	$10^{4.8}$	L/kg	(*77–79*)
Biochar-water partitioning coefficient PFOA	$K_{f\ PFOA}$	Sorption coefficient of PFOA on biochar	$10^{3.3}$	L/kg	(*77–79*)
Log-SD of Kd (PFOS/PFOA)	$\sigma_{log\ Kd}$	Standard deviation on log-scale for Kd sampling	0.10/0.15	L/kg	(*77–79*)
Initial PFOS soil concentration	$C_{soilPFOS}$	PFOS concentration in Year 0 soil	100	ng/g	Representing >90 percentile
Initial PFOA soil concentration	$C_{soilPFOA}$	PFOA concentration in Year 0 soil	4	ng/g	Average site conditions

Table S4. Summary table for literature results of biochar addition to soils and plant uptake dynamic or leaching behavior.

Biochar	Plant	Soil Type	Application Rate	PFAS/ PFOS Uptake	Source
Black Owl Biochar Environmental Ultra™	Grass-Legume (9 varieties)	Silt loam, Silty Clay Loam	0%, 0.05%, 0.2%, 1%	Stabilized at 1% biochar. Increased uptake at low doses (0.05%)	Ilango et. al, 2024(*24*)
Organic custom wood and grass derived	Grass-Legume (9 varieties)	Silt Loam, Silty clay loam	0%, 0.05%, 0.2%, 1%	Stabilized at 1% biochar	Ilango et. al, 2024(*24*)
Luna s.r.l	Tomato (*Lycopersicum esculentum Mill., cv. Roma*)	Clay Loam	3%*	Reduction in leaves (-45% - -84%), fruits -61%.	Battisti et. al, 2024(*68*)
Luna s.r.l	Red Chicory (*Cychorium intybus L., cv.* late Treviso)	Clay Loam	3%*	Reduction in leaves (-74%), increase in soil for all PFAS.	Battisti et. al, 2024(*68*)
Forest Wood Waste	Timothy-grass	Sandy loam	0.2% , 2%	Increased plant uptake by 120% in 0.2% amended soil. Decreased leachable PFAS from soil.	Zhang et al 2022(*69*)
Granular activated carbon	Timothy-grass	Sandy loam	0.2% , 2%	Total PFAS concentration in grass shoots was 2.77% of grass from non-amended soil.	Zhang et al 2022(*69*)
Waste-Based (clean wood chips, waste timber, activated waste timber, digested sewage and dewatered raw sewage)	-	Sandy	1%	PFOS leachate concentration reduced by 99.9% with activated waste timber biochar at 1%.	Sørmo et. al, 2024(*67*)
Pine	-	Loamy Sand, Sandy Clay Loam	0-5%	Effect higher in sandy clay loam (sorption 69.8±4.9%) than loamy sand (sorption 11±4.5%)	Askeland et. al, 2020(*80*)
Waste timber	-	Moraine	5%	98-100% reduction in leachate concentration in low TOC soil, 23-100% reduction for high TOC.	Sørmo et. al, 2021(*78*)

* Calculated with an estimated soil density = 1300 kg/m^3

Table S5. Parameters, values, and sources for the calculation of the amount of concentration of PFOS in pasture grass which meets risk based thresholds in equation X

Parameter	Description	Value	Units	Source
C_{soil}	Soil screening level (hay-based farm scenario)	6,800	ng/kg dry soil	(*27*)
TF_{plant}	Soil-to-plant transfer factor (hay)	0.07	unitless	(*27*, *81*)
MLF	Soil mass loading factor (soil on hay surface)	0.034	g dry soil / g dry plant	(*70*)
C_{plant}	Back-calculated plant concentration (threshold)	707	ng/kg dry plant	Calculated

Table S6. Values for biomass yields and conversations of biomass to biochar

Parameter	Symbol	Distribution	Range	Units	Source
Biomass yield	Y_b	Linear with latitude	10–25	tons ha^{-1} yr^{-1}	(*82*)
Biochar conversion efficiency	η	Uniform	0.15–0.30	dimensionless	(*83*)
Biochar C content	C_f	Uniform	0.60–0.80	dimensionless	(*72*)
Area grid cell	A	Determined	1,000	ha	-

Table S7. The parameters, values, and sources for the calculation of emissions from the traditional remediation of PFAS impacted land

Parameter	Symbol	Description	Range	Units	Source/Notes
Full Capacity Fuel Efficiency Range	F_F	Efficiency of diesel fuel for a full semi truck	8.73355 – 10.919	km/gal	(*84*)
Diesel Emissions	E_d	Emissions from diesel fuel.	0.01018	t/gal	(*85*)
Truck Load	L_T	Maximum load of semi truck	23 – 24	t	(*86*)
Landfill Distance	d_l	Distance in km to the nearest landfill for hazardous material.	322 – 805	km	Estimated
Rotary Kiln Distance	d_k	Distance in km to the nearest rotary kiln.	362 – 402	km	Estimated
Soil Depth	s_d	Average soil depth of contamination removal.	0.30	m	(*87*)
Soil Density	ρ_s	Average soil density.	1.3	t/m^3	(*66*)
Rail emission factor	E_r	CO_2 emissions per ton-km (rail)	2.1×10^{-5}	$tCO_2/(t\cdot km)$	(*88*)
Deadhead distance	d_d	Reposition distance for next job	16–64	km	Estimated
OM fraction in soil	f_{OM}	Organic matter mass fraction of soil	1–3.5%	%	(*89*)
C fraction of OM	$f_{C\|OM}$	Carbon fraction within OM	40–60%	%	(*90*, *91*)
Energy use per ton	ε_E	Kiln energy consumption	0.5–2.0	MMBtu/t	(*92*)
Rail switch threshold	d_s	Distance above which rail is used	120	km	Estimated
BTU Usage	u_{BTU}	Range of hourly BTU consumption of a rotary kiln	10-100	MMBtu/hr	(*93*)
Emissions per BTU	E_{BTU}	Emissions of CO_2 per million BTUs used during the operation of a rotary kiln.	116.65	Lbs CO_2/MMBtu	(*93*, *94*)
Kiln Processing Capacity	c_k	Average capacity of a kiln to pyrolyze contaminated soil.	22	t/hr	(*92*, *95*)
Average Farm Size	a_f	Average farm size in the United States	180	ha	(*96*)
Hazardous waste disposal cost	C_{lf}	Average price of soil disposal	277	USD / ton	(*16*)
Thermal treatment cost	C_{kn}	Average price of thermal treatment of soil	510	USD / ton	(*16*)

Table S8. Model parameters for Monte Carlo simulation of biochar cost

Parameter	Symbol	Description	Range	Units	Source/Notes
Consumption rate: large	B_L	Maximum hourly biomass consumption	2.5 – 4.5	t/hr	(*97*), quote estimates
Consumption rate: mobile	B_M	Maximum biomass capacity of mobile pyrolysis rig	1 – 2	t/hr	(*98*, *99*)
Operating hours: large	T_L	Hours of operation per day.	10 – 24	hr	Based on facility production estimates
Operating hours: mobile	T_M	Hours of operation per day.	6-10	hr	Based on labor
Biomass to biochar	b_{BC}	Tons of biochar produced from one ton of biomass	0.20-0.25	-	(*98–100*)
Carbon content	C_{BC}	Fraction of carbon in biochar.	0.70 – 0.95	-	(*100*, *101*)
Biomass cost	P_B	Price of biomass per ton	0 – 70	$/t	(*102*)
Fuel efficiency range	F_F	Efficiency of diesel fuel for a full semi-truck	8.73355 – 10.919	km/gal	(*103*, *104*)
Average fuel consumption	F_M	Average fuel consumption of a mobile pyrolysis unit.	1.1	gal/hr	(*98*, *99*)
Diesel emissions	E_d	Emissions from diesel fuel.	0.01018	t/gal	(*105*)
Average fuel price	P_{fuel}	Average price of diesel fuel in USD.	3.67	$	(*106*)
Operating cost: large pyrolysis	O_L	Cost per hour of operating a large pyrolysis plant.	0-250	$/hr	Quote estimates.
Operating cost: mobile unit	O_M	Cost per hour of operating a mobile pyrolysis unit.	50	$/hr	Quote estimates.
Cost for mobile pyrolysis	P_M	Cost for the capital investment	200,000 – 360,000	$	Quote estimates.
Truck load	L_T	Maximum load of semi-truck	23 – 24	t	(*107*)
Driving distance	d_t	Distance in km material moved by truck.	50 – 200	km	Quote estimates
Trucking operating cost	P_{km}	Per-distance trucking operating cost	1.364 - 3.115	$/km	(*108*)

Table S9. Parameters, values, and sources for the economic costs analysis

Parameter	Symbol	Range / Mean ± SD	Units	Source
Simulation years	T	22.5 ± 4.5	yr	Calculated
Fescue production cost	C_{fescue}	550–780	USD ha^{-1} yr^{-1}	(*109*, *110*)
Hemp production cost	C_{hemp}	750–900	USD ha^{-1} yr^{-1}	(*111*)
Farmer income offset	I_{farmer}	300–500	USD ha^{-1} yr^{-1}	Estimated
Biochar CDR rate	$Q_{biochar}$	4.8–16.5	tCO_2 ha^{-1} yr^{-1}	Calculated
ERW CDR rate	Q_{ERW}	2–6	tCO_2 ha^{-1} yr^{-1}	(*42*, *112*)
Biochar cost rate	$P_{biochar}$	133 ± 43	USD tCO_2^{-1}	Calculated
ERW cost rate	P_{ERW}	160–180	USD tCO_2^{-1}	(*42*)
Biochar sale price	$S_{biochar}$	125–175	USD tCO_2^{-1}	(*40*)
ERW sale price	S_{ERW}	300–325	USD tCO_2^{-1}	(*40*)
Social Cost Carbon	SCC	190-275	USD tCO_2^{-1}	(*41*)